NASA Technical Memorandum **107758**

THE ADDITION OF ALGEBRAIC TURBULENCE MODELING TO PROGRAM LAURA

F. McNeil Cheatwood

R. A. Thompson

APRIL 1993

NASA

National Aeronautics and Space Administration

Langley Research Center
Hampton, Virginia 23681-0001

The Addition of Algebraic Turbulence Modeling to Program LAURA

F. McNeil Cheatwood Vigyan, Inc.
Hampton, VA 23665-0325

R. A. Thompson NASA Langley Research Center
Hampton, VA 23681-0001

Summary

The Langley Aerothermodynamic Upwind Relaxation Algorithm (LAURA) is modified to allow the calculation of turbulent flows. This is accomplished using the Cebeci-Smith and Baldwin-Lomax eddy-viscosity models in conjunction with the thin-layer Navier-Stokes options of the program. Turbulent calculations can be performed for both perfect-gas and equilibrium flows. However, a requirement of the models is that the flow be attached. It is seen that for slender bodies, adequate resolution of the boundary-layer gradients may require more cells in the normal direction than a laminar solution, even when grid stretching is employed. Results for axisymmetric and three-dimensional flows are presented. Comparison with experimental data and other numerical results reveal generally good agreement, except in the regions of detached flow.

Introduction

With the continuing interest in hypersonics, and the associated desire to model more complex phenomena of the flowfields about bodies in hypersonic flight, numerical solvers of the full Navier-Stokes equations are being employed with increasing regularity. Ongoing advancements in numerical algorithms and computer hardware have made this feasible. Specific applications include full-flowfield calculations about complex configurations such as the Space Shuttle [1, 2] and National Aero-Space Plane (NASP) [3, 4], with their associated high altitude, high speed environments. Development of the various numerical models necessary to simulate the physical processes in these environments is an important part of this capability. At high Reynolds number conditions, turbulent flow is one process which becomes important, and its numerical simulation is the subject of this work.

Solving the full Navier-Stokes equations is required to accurately predict most complicated continuum flowfields. Typically the unsteady form of the Navier-Stokes equations are solved using a time-marching procedure. This allows any elliptic behavior to be properly modeled, but at a price: Navier-Stokes solutions are significantly more computation-intensive than solutions from less detailed methods which do not involve time relaxation procedures. The thin-layer approximation to the Navier-Stokes equations may be employed (to eliminate

the viscous terms containing derivatives in the streamwise direction), but the solution is still quite expensive. Still, for complex flowfields with separation and large subsonic regions, there is little choice but to solve the full or thin-layer Navier-Stokes equations.

The Langley Aerothermodynamic Upwind Relaxation Algorithm (LAURA) is a three-dimensional finite-volume Navier-Stokes solver developed by Gnoffo [5-8]. LAURA was initially applied to blunt-body flows, but has been used with slender bodies [9, 10] as well. This paper serves as a follow-up to reference 10 which used LAURA for aerothermodynamic predictions over slender vehicles assuming laminar, perfect-gas flow. In this work, turbulent flows over slender bodies will be modeled.

In various efforts [11-13] eddy-viscosity models have been mated with existing flowfield solvers. The Cebeci-Smith [14-16] and Baldwin-Lomax [17] eddy-viscosity models are employed here. Such algebraic (or zero-equation) models are less complicated than more exact approaches, such as the Johnson-King [18] and two-equation [13] models, and as a result are more computationally efficient (although theoretically less accurate). The thin-layer Navier-Stokes option of LAURA is exercised in this study. For implementation in LAURA, several issues must be addressed: 1) the actual modeling of the turbulence, 2) the resolution of near-body gradients, and 3) the transition from laminar to turbulent flow.

In this study, both perfect-gas and equilibrium flow conditions are considered. Calculations are performed for sphere-cones and a generic transatmospheric vehicle (TAV). The LAURA heat-transfer predictions are compared with experimental data, as well as other numerical calculations, in order to evaluate the present results. In the sections that follow, brief discussions of the LAURA computational method, along with the modifications employed for turbulent calculations, are given. A discussion of the results and some conclusions from this study follow.

List of Symbols

a	Speed of sound
C_p	Specific heat at constant pressure
$\hat{e}_s$	Unit vector in s-direction
$\hat{e}_\phi$	Unit vector in ϕ-direction
h	Static enthalpy
H	Total enthalpy; $H = h + V^2/2$
k	Thermal conductivity
L	Reference length of body
M	Mach number
n	Normal distance from the body
Δn	Height or thickness of cell (in n-direction)
n^+	Normal coordinate parameter for turbulent flow
Pr	Prandtl number; $Pr = \mu C_p/k$
q	Heat transfer rate
Re_{cell}	Cell Reynolds number; $Re_{cell} = \rho a \Delta n/\mu$
s	Surface distance along the body, measured from its nose
T	Temperature
u, v, w	Velocity components in the s-, n-, ϕ-directions, respectively

V	Total velocity; $V^2 = V_x^2 + V_y^2 + V_z^2 = u^2 + v^2 + w^2$
V_x, V_y, V_z,	Velocity components in the x-, y-, z-directions, respectively
x, y, z	Cartesian coordinates with origin at body nose
δ	Value of n at boundary-layer edge
$\delta^\star$	Boundary-layer displacement thickness
ε^+	Ratio of eddy viscosity to laminar viscosity; $\varepsilon^+ = \mu_t/\mu$
μ	Dynamic viscosity
ρ	Density
ϕ	Angular coordinate in the circumferential direction around the body
τ	Shear stress
ω	Vorticity

Subscripts

e	Boundary-layer edge
t	Turbulent value
w	Wall value
∞	Freestream condition

Computational Method

LAURA is a finite-volume formulation of the integral form of the Navier-Stokes equations. A second-order accurate, symmetric total-variation-diminishing (STVD) scheme [19] is used in conjunction with the upwinded differencing of the discretized equations. At each cell face, Roe's averaging [20] defines the flowfield variables based on values from the adjacent cells. The unsteady governing equations are driven to a steady-state solution through a time relaxation procedure involving global sweeps through the computational domain. In the relaxation scheme, dependent variables at a cell center are treated implicitly, using the latest available information from adjacent cells. Thus, for perfect-gas flow, the relaxation simply requires the inversion of a 5×5 matrix at each cell center.

During the relaxation process, the grid is periodically adapted in the body-normal direction so that the grid can be tailored to the emerging solution. This process of customizing the mesh involves clustering the cells near the body surface for accurate heat-transfer calculations. In addition, the outer boundary of a converged grid is parallel to the captured bow-shock wave. A later section provides more details of this process.

Typically, calculations begin with a grid which has only one-fourth the total number of cells in the normal direction. The use of this coarse grid allows even a poor initial guess for the mesh to quickly align itself with the developing bow shock with repeated adaptions of the normal distribution. The density of cells in the normal direction is later increased by factors of two during the relaxation sweeps. This process promotes convergence and stability of the solution.

For future reference, the STVD limiter given by equation (3.8b) of reference 7 was used for the results presented later. Further, for the present calculations, an eigenvalue limiter of 0.3 was used in all directions. For the normal direction, the limiter is scaled according to the cell aspect ratio so that the resultant limiter approaches zero near the body. As a result,

the viscous terms containing derivatives in the streamwise direction), but the solution is still quite expensive. Still, for complex flowfields with separation and large subsonic regions, there is little choice but to solve the full or thin-layer Navier-Stokes equations.

The Langley Aerothermodynamic Upwind Relaxation Algorithm (LAURA) is a three-dimensional finite-volume Navier-Stokes solver developed by Gnoffo [5-8]. LAURA was initially applied to blunt-body flows, but has been used with slender bodies [9, 10] as well. This paper serves as a follow-up to reference 10 which used LAURA for aerothermodynamic predictions over slender vehicles assuming laminar, perfect-gas flow. In this work, turbulent flows over slender bodies will be modeled.

In various efforts [11-13] eddy-viscosity models have been mated with existing flowfield solvers. The Cebeci-Smith [14-16] and Baldwin-Lomax [17] eddy-viscosity models are employed here. Such algebraic (or zero-equation) models are less complicated than more exact approaches, such as the Johnson-King [18] and two-equation [13] models, and as a result are more computationally efficient (although theoretically less accurate). The thin-layer Navier-Stokes option of LAURA is exercised in this study. For implementation in LAURA, several issues must be addressed: 1) the actual modeling of the turbulence, 2) the resolution of near-body gradients, and 3) the transition from laminar to turbulent flow.

In this study, both perfect-gas and equilibrium flow conditions are considered. Calculations are performed for sphere-cones and a generic transatmospheric vehicle (TAV). The LAURA heat-transfer predictions are compared with experimental data, as well as other numerical calculations, in order to evaluate the present results. In the sections that follow, brief discussions of the LAURA computational method, along with the modifications employed for turbulent calculations, are given. A discussion of the results and some conclusions from this study follow.

List of Symbols

a	Speed of sound
C_p	Specific heat at constant pressure
$\hat{e}_s$	Unit vector in s-direction
$\hat{e}_\phi$	Unit vector in ϕ-direction
h	Static enthalpy
H	Total enthalpy; $H = h + V^2/2$
k	Thermal conductivity
L	Reference length of body
M	Mach number
n	Normal distance from the body
Δn	Height or thickness of cell (in n-direction)
n^+	Normal coordinate parameter for turbulent flow
Pr	Prandtl number; $Pr = \mu C_p/k$
q	Heat transfer rate
Re_{cell}	Cell Reynolds number; $Re_{cell} = \rho a \Delta n/\mu$
s	Surface distance along the body, measured from its nose
T	Temperature
u, v, w	Velocity components in the s-, n-, ϕ-directions, respectively

Conductivity is also affected by turbulence. For laminar flow,

$$q = \frac{k}{C_p}\frac{\partial h}{\partial n} \tag{8}$$

Accounting for the turbulent contribution gives

$$q = \frac{(k + k_t)}{C_p}\frac{\partial h}{\partial n} \tag{9}$$

where k_t is the eddy thermal conductivity. By definition,

$$Pr = \frac{C_p \mu}{k}$$

so that

$$\frac{k}{C_p} = \frac{\mu}{Pr} \qquad \text{and} \qquad \frac{k_t}{C_p} = \frac{\mu_t}{Pr_t}$$

Thus,

$$\frac{k}{C_p} + \frac{k_t}{C_p} = \frac{\mu}{Pr} + \frac{\mu_t}{Pr_t} = \frac{\mu}{Pr}\left(1 + \frac{\mu_t}{\mu}\frac{Pr}{Pr_t}\right)$$

While in general the value of Pr_t varies throughout the shock layer, a constant value of 0.9 is commonly used.

Defining the ratio of eddy viscosity to laminar viscosity as

$$\varepsilon^+ = \frac{\mu_t}{\mu} \tag{10}$$

gives the final form of the modifications to the governing equations:

$$\mu \Longrightarrow \mu\left(1 + \varepsilon^+\right) \qquad \frac{\mu}{Pr} \Longrightarrow \frac{\mu}{Pr}\left(1 + \varepsilon^+\frac{Pr}{Pr_t}\right)$$

Note that for laminar flow, $\mu_t = 0$ and $k_t = 0$.

The Cebeci-Smith and Baldwin-Lomax algebraic models are two-layer eddy-viscosity formulations which are applicable to attached flows. The inner-layer value, ε_i^+, is based on Prandtl's mixing length concept [22]. For Cebeci-Smith, the outer layer value, ε_o^+, is given by the Clauser-Klebanoff [23, 24] expression. The Baldwin-Lomax model uses an equivalent expression for ε_o^+, but differs in its determination of the length scale. For both models, the inner-layer expression is used from the wall outward until $\varepsilon_i^+ > \varepsilon_o^+$, thus forming a composite eddy viscosity. Details of each of these models are given below.

Cebeci-Smith

As mentioned above, the inner-layer eddy viscosity is based on Prandtl's mixing length theory:

$$\varepsilon_i^+ = \frac{\rho l^2}{\mu}\left|\frac{\partial \vec{U}}{\partial n}\right| \tag{11}$$

The mixing length for the inner layer according to Van Driest [22] is

$$l = K_v n \left[1 - exp\left(-n^+/A^+\right)\right] \tag{12}$$

where the von Karman constant is

$$K_v = 0.4$$

and the normal coordinate parameter is

$$n^+ = \frac{n\rho}{\mu}\left[\frac{\tau_w}{\rho}\right]^{1/2} \tag{13}$$

In reference 25, the damping factor is defined as

$$A^+ = 26\left(\left|\frac{\tau}{\tau_w}\right|\right)^{-1/2} \tag{14}$$

where the local shear stress is

$$\tau = \mu\left(1 + \varepsilon^+\right)\left|\frac{\partial \vec{U}}{\partial n}\right| \tag{15}$$

and

$$\tau_w = \mu_w \left|\frac{\partial \vec{U}}{\partial n}\right|_w \tag{16}$$

The outer layer eddy viscosity is approximated by the Clauser-Klebanoff [23, 24] expression:

$$\varepsilon_o^+ = 0.0168\, U_e\, \delta^\star\, \frac{\rho\, \gamma_{i,n}}{\mu} \tag{17}$$

The displacement thickness is

$$\delta^\star = \int_0^\delta \left(1 - \frac{U}{U_e}\right) dn \tag{18}$$

where δ is the value of n at the boundary-layer edge. By definition, at the boundary-layer edge,

$$\frac{H}{H_\infty} \rightarrow 1$$

Numerically, this can be approximated as the grid point where

$$\frac{H}{H_\infty} > 0.995$$

The normal intermittency factor is

$$\gamma_{i,n} = \left[1 + 5.5\left(\frac{n}{\delta}\right)^6\right]^{-1} \tag{19}$$

The mixing length for the inner layer according to Van Driest [22] is

$$l = K_v n \left[1 - exp\left(-n^+/A^+\right)\right] \tag{12}$$

where the von Karman constant is

$$K_v = 0.4$$

and the normal coordinate parameter is

$$n^+ = \frac{n\rho}{\mu}\left[\frac{\tau_w}{\rho}\right]^{1/2} \tag{13}$$

In reference 25, the damping factor is defined as

$$A^+ = 26\left(\left|\frac{\tau}{\tau_w}\right|\right)^{-1/2} \tag{14}$$

where the local shear stress is

$$\tau = \mu\left(1 + \varepsilon^+\right)\left|\frac{\partial \vec{U}}{\partial n}\right| \tag{15}$$

and

$$\tau_w = \mu_w \left|\frac{\partial \vec{U}}{\partial n}\right|_w \tag{16}$$

The outer layer eddy viscosity is approximated by the Clauser-Klebanoff [23, 24] expression:

$$\varepsilon_o^+ = 0.0168\, U_e\, \delta^*\, \frac{\rho\, \gamma_{i,n}}{\mu} \tag{17}$$

The displacement thickness is

$$\delta^* = \int_0^\delta \left(1 - \frac{U}{U_e}\right) dn \tag{18}$$

where δ is the value of n at the boundary-layer edge. By definition, at the boundary-layer edge,

$$\frac{H}{H_\infty} \rightarrow 1$$

Numerically, this can be approximated as the grid point where

$$\frac{H}{H_\infty} > 0.995$$

The normal intermittency factor is

$$\gamma_{i,n} = \left[1 + 5.5\left(\frac{n}{\delta}\right)^6\right]^{-1} \tag{19}$$

Baldwin-Lomax

The expression for the inner-layer eddy viscosity in the Baldwin-Lomax model is similar to that used in the Cebeci-Smith model:

$$\varepsilon_i^+ = \frac{\rho l^2}{\mu} |\omega| \tag{20}$$

The mixing length, l, is again given by equation 12 in conjunction with equations 13 through 16. The magnitude of the vorticity, $|\omega|$, is found from

$$|\omega| = \left\{ \left[\frac{dV_z}{dy} - \frac{dV_y}{dz} \right]^2 + \left[\frac{dV_z}{dx} - \frac{dV_x}{dz} \right]^2 + \left[\frac{dV_y}{dx} - \frac{dV_x}{dy} \right]^2 \right\}^{\frac{1}{2}} \tag{21}$$

$$= \left\{ \left[\frac{dw}{dn} - \frac{dv}{d\phi} \right]^2 + \left[\frac{dw}{ds} - \frac{du}{d\phi} \right]^2 + \left[\frac{dv}{ds} - \frac{du}{dn} \right]^2 \right\}^{\frac{1}{2}}$$

For thin-layer Navier-Stokes, this becomes

$$|\omega| = \left\{ \left[\frac{dw}{dn} \right]^2 + \left[\frac{du}{dn} \right]^2 \right\}^{\frac{1}{2}} \tag{22}$$

The outer layer eddy viscosity is approximated by the Clauser-Klebanoff [23, 24] expression:

$$\varepsilon_o^+ = 0.0168 \, C_{CP} \, F_{max} \, n_{max} \, \frac{\rho \, \gamma_{i,n}}{\mu} \tag{23}$$

where $n = n_{max}$ is the location of the maximum value, F_{max}, of the vorticity function:

$$F = n \, |\omega| \left[1 - exp\left(-n^+ / A^+ \right) \right] \tag{24}$$

Although a Mach number dependency has been suggested for C_{CP} (see ref. 25), in the results presented later, a constant value of $C_{CP} = 1.6$ as given in reference 17 yields the best agreement. Klebanoff's intermittency factor is

$$\gamma_{i,n} = \left[1 + 5.5 \left(\frac{C_{KLEB} \, n}{n_{max}} \right)^6 \right]^{-1} \tag{25}$$

where $C_{KLEB} = 0.3$.

The boundary-layer thickness does not appear in the Baldwin-Lomax model. The length scale of the outer layer is instead based on F_{max}, the maximum of the vorticity function. Since the solution is discretized, the position and value of this maximum can be "smeared". In an effort to minimize this behavior, the discrete values in the vicinity of the maximum are curve-fit using an "overlapping-parabola" technique. The result of this process can be seen in the sample streamwise distributions shown in the figures which follow. Figure 1 shows that the process has little effect on F_{max} itself. However, figure 2 shows that the position of this maximum is a more sensitive quantity. Note the "jump" at $s \approx 4$ which is present when the parabolic blending is not used. Since it is the product of these terms, $F_{max} n_{max}$, which appears in equation 23, the calculated eddy viscosity will reflect such "jumps". Figure 3 illustrates this effect on the near-body ε^+-distributions in the vicinity of a jump in n_{max}. Note that the streamwise variation in the ε^+-profiles is much smoother when parabolic-blending is employed.

where $Re_{cell,w}$ is the desired cell Reynolds number at the body and n_K is the distance from the body to the outer grid boundary. The value of n_K is "lagged" from the previous grid. In past investigations [10], a wall value of $Re_{cell,w} = \mathcal{O}(1)$ at the wall has proved to be adequate for laminar heating rates.

The objective is to adequately resolve the boundary-layer gradients without overly-resolving the outer shock layer where gradients are small. Thus, grid stretching is used near the body, in conjunction with even spacing in the outer region of the grid. The spacing from these two regions are constrained to match at their interface. The fraction of the total cells used in the stretched region is given by

$$F_{str} = \max\left(\frac{1}{2} \ , \ 1 - \frac{32}{K} \right) \tag{31}$$

where K is the total number of cells in the normal direction. The number of stretched cells for this normal line is

$$K_{str} = F_{str} K \tag{32}$$

The recursion formula for the nondimensional height of these K_{str} cells, using a sinusoidal distribution, is

$$\Delta\tilde{n}_k = \left\{ 1 + f_{str} \sin\left[\frac{(k-1)\,\pi}{K_{str} - 1} \right] \right\} \Delta\tilde{n}_{k-1} \tag{33}$$

where

$$f_{str} = \left[\frac{F_{str}}{\Delta\tilde{n}_1} \right]^{\frac{1}{K_{str}}} - 1 \tag{34}$$

The total nondimensional distance from the body to the outer edge of any cell k is found from

$$\tilde{n}_k = \sum_{l=1}^{k} \Delta\tilde{n}_l \tag{35}$$

This distribution is then normalized to yield $0 \leq \tilde{n} \leq 1$.

In this investigation, it was found that the above normal distribution did not always adequately resolve the turbulent boundary layer. Apparently, the cell Reynolds number at the wall must be more tightly matched to the target value of $Re_{cell,w} = 1$. To achieve this, the value of f_{str} is determined iteratively for each stack of cells, with the value from equation 34 serving as an initial guess. The resultant iterated value of f_{str} yields $\hat{n}_K \approx 1$ so that $Re_{cell,w} \approx 1$ at the wall.

Another quantity useful in gauging adequate grid resolution for turbulent flows is the wall value of the normal coordinate parameter (n_w^+). As a rule of thumb, its value should not be larger than $\mathcal{O}(0.1)$ for proper resolution of the turbulent boundary-layer gradients. Using a target value of $n_w^+ = 0.1$, this yields another expression for the thickness of the cell adjacent to the body:

$$\Delta\tilde{n}_1 = \frac{n_w^+}{n_1^+} \frac{n_1}{n_K} \tag{36}$$

where, from equation 13,

$$n_1^+ = \frac{\hat{n}_1 \rho_1}{\mu_1} \left[\frac{\tau_w}{\rho_1} \right]^{1/2}$$

Note that $\hat{n}_1$ is the distance from the body to the center of cell 1, so that $n_1 = 2\hat{n}_1$.

Both equations 30 and 36 provide values for $\Delta\tilde{n}_1$, and so the smallest of these two values is used to define the thickness of any cell adjacent to the body. With the proper stretching determined, dimensionality is returned to the distribution by

$$n_k = \frac{n_s}{F_s}\tilde{n}_k \tag{37}$$

where n_s is the distance from the body to the bow shock for this stack of cells (lagged from the previous grid). The fraction of the distance from the body to the outer grid boundary which lies between the bow shock and body is given by F_s. A value of $F_s = 0.8$ is used here so that with a converged grid, the distance across the shock layer is eighty percent of the total distance from the body to the outer (freestream) boundary.

Implementation

The turbulence models used here require a fairly developed shock layer for implementation. Therefore, for all the cases presented herein, the LAURA code is run for laminar flow until the residual drops several orders of magnitude. At this point (before the laminar solution is fully converged), the turbulence is "turned on" and the iteration process is continued. Not surprisingly, the switch from laminar to turbulent flow results initially in a jump in the residual. After a period of adjustment to the new governing equations, the residual again begins to steadily decrease. The rate of this decrease is less than for laminar flow, since the higher viscosity for turbulent flow serves as damping for the solution. Figure 4 gives a typical residual history. In addition to the rise with the switch from laminar to turbulent flow, "jumps" in the residual occur when the grid is adapted.

The LAURA package has several features which enable it to handle very large jobs and utilize multiple processors when running on CRAY supercomputers. For instance, the computational domain can be divided into several "blocks" with information communicated across their boundaries. The work within a given block (or for the entire domain) may be allocated to several processors. Although the results are not included here, the turbulence programming has been successfully tested in conjunction with both of these features.

Solving the governing equations for turbulent flow increases the required computational time by approximately 1.5 percent per iteration per grid cell as compared with laminar calculations. However, since the turbulent terms increase the damping, more iterations are required to drive a turbulent solution to the same level of convergence as a laminar solution. Storage requirements for the LAURA code are also increased slightly since values for the eddy viscosity and normal distance from the body must be saved for each cell in the grid. In addition, the distance along the body surface to each wall-bounded cell is required to define the transition region.

Results and Discussion

In an effort to verify proper implementation of the turbulence models within LAURA, several test cases were computed. The results are given below in order of increasing complexity. The first case is an axisymmetric, perfect-gas flowfield calculation which is compared

with experimental data. The second is an axisymmetric, equilibrium flow case which is compared with results from another numerical approach. Finally, results for perfect-gas flow over a three-dimensional body are compared with experimental data. The results presented here are restricted to heating-rate comparisons. Specifically, streamwise heating rates (normalized by a reference rate) are plotted as a function of axial distance from the body nose (nondimensionalized by a reference length). For the three-dimensional case, circumferential heating rates for selected stations are included, plotted versus spanwise distance from the symmetry plane.

Perfect Gas

The first case is a Mach 5 perfect-gas flowfield calculation over an 8-*deg* sphere-cone at 0-*deg* angle of attack. Comparisons are made with Jackson's experimental data [29]. The geometry has a length of $L = 25.4cm$ $(10in)$ and a nose radius of $R_{nose} = 6.35cm$ $(2.5in)$. The freestream conditions are $\rho_\infty = 0.48\ kg/m^3$ and $T_\infty = 111.1\ K$. Jackson's data include body temperature measurements, so a variable wall temperature is specified. The transition point is specified to be $s = 2.54cm$ $(1in)$. Calculations using both the Cebeci-Smith and Baldwin-Lomax models are presented. The computations were performed on a workstation with 41 cells used in the axial direction.

The baseline LAURA code can readily accommodate increases in the number of cells in the normal (k) direction. However, these increases are limited to grid doubling. For example, if 64 cells do not yield a satisfactory solution, then the grid may be doubled to 128 cells. For this investigation, the doubling routine has been modified so that any increase in the number of cells in the normal direction may be performed easily. To reduce computational costs, LAURA starts the solution for each new number of cells from the previous solution, rather than restarting from conditions based on freestream values.

The heating results of a grid refinement study (using the Cebeci-Smith model only) are presented in figure 5, where $q_{ref} = 340\ kW/m^2\ (30\ BTU/s/ft^2)$. The condition of $Re_{cell,w} = 1$ is enforced for all solutions shown in the figure. Recall that the total number of cells (K) dictates the value of K_{str}, the number of cells in the near-wall region (see equations 31 and 32). Apparently, for this slender body, a value of $K_{str} > 48$ is required to obtain a grid converged prediction of the turbulent heating. If a value of $K_{str} \leq 48$ is used, a grid which extends out far enough to encompass the bow shock while maintaining $Re_{cell,w} = 1$ is overly stretched. To further illustrate this point, table 1 gives the maximum stretching $(1 + f_{str})$ associated with each normal cell distribution represented in figure 5. Although this maximum stretching does not occur at the wall (see equation 33), it does lie within the boundary layer. It is seen that for this slender body, the $K = 96$ solution is essentially the same as the $K = 128$ solution. This is significant since the 128-cell solution requires approximately one-third more time to run than the 96-cell result. One can infer from these results that a maximum stretching of approximately 1.25 is desirable. However, the allowable maximum stretching may vary from case to case. In general, the best approach for a given case is to repeat such a grid resolution study. It should be noted that although a criterion for $n_w^+ = 0.1$ is also employed, for the results presented in this paper, $Re_{cell,w} = 1$ proves to be the more strict control for these conditions.

With the flowfield initialized to the 96-cell Cebeci-Smith results, the solution is recalculated using the Baldwin-Lomax model. Figure 6 contrasts both numerical solutions with the

Note that $\hat{n}_1$ is the distance from the body to the center of cell 1, so that $n_1 = 2\hat{n}_1$.

Both equations 30 and 36 provide values for $\Delta\tilde{n}_1$, and so the smallest of these two values is used to define the thickness of any cell adjacent to the body. With the proper stretching determined, dimensionality is returned to the distribution by

$$n_k = \frac{n_s}{F_s}\tilde{n}_k \tag{37}$$

where n_s is the distance from the body to the bow shock for this stack of cells (lagged from the previous grid). The fraction of the distance from the body to the outer grid boundary which lies between the bow shock and body is given by F_s. A value of $F_s = 0.8$ is used here so that with a converged grid, the distance across the shock layer is eighty percent of the total distance from the body to the outer (freestream) boundary.

Implementation

The turbulence models used here require a fairly developed shock layer for implementation. Therefore, for all the cases presented herein, the LAURA code is run for laminar flow until the residual drops several orders of magnitude. At this point (before the laminar solution is fully converged), the turbulence is "turned on" and the iteration process is continued. Not surprisingly, the switch from laminar to turbulent flow results initially in a jump in the residual. After a period of adjustment to the new governing equations, the residual again begins to steadily decrease. The rate of this decrease is less than for laminar flow, since the higher viscosity for turbulent flow serves as damping for the solution. Figure 4 gives a typical residual history. In addition to the rise with the switch from laminar to turbulent flow, "jumps" in the residual occur when the grid is adapted.

The LAURA package has several features which enable it to handle very large jobs and utilize multiple processors when running on CRAY supercomputers. For instance, the computational domain can be divided into several "blocks" with information communicated across their boundaries. The work within a given block (or for the entire domain) may be allocated to several processors. Although the results are not included here, the turbulence programming has been successfully tested in conjunction with both of these features.

Solving the governing equations for turbulent flow increases the required computational time by approximately 1.5 percent per iteration per grid cell as compared with laminar calculations. However, since the turbulent terms increase the damping, more iterations are required to drive a turbulent solution to the same level of convergence as a laminar solution. Storage requirements for the LAURA code are also increased slightly since values for the eddy viscosity and normal distance from the body must be saved for each cell in the grid. In addition, the distance along the body surface to each wall-bounded cell is required to define the transition region.

Results and Discussion

In an effort to verify proper implementation of the turbulence models within LAURA, several test cases were computed. The results are given below in order of increasing complexity. The first case is an axisymmetric, perfect-gas flowfield calculation which is compared

near-wall region. As a result, differences in the equilibrium models are not as significant as they were for the laminar results. Since the same eddy viscosity model is used for all of these techniques, and this is the dominant viscosity in the boundary layer, the turbulent results from these two algorithms should be in good agreement. This is in fact the case, as shown in figure 7, where the turbulent results are seen to be within approximately five percent of one another.

The LAURA results presented for this case are generated using 128 cells in the normal direction. The maximum stretching is approximately 1.1 and occurs at the end of the body. Although not shown, this solution agrees well (within five percent) with a solution using 96 cells in the normal direction, whose maximum stretching is nearly 1.2. This close agreement between the results for two grids indicates that the solution is grid-converged.

Three-Dimensional Flow

The third and final case is perfect-gas flow over a generic TAV configuration, which is depicted in figure 8. This blended wing-body (BWB) configuration is a three-dimensional vehicle which features nose bluntness, a flattened windward surface, leading edge chines, and a double compression ramp system. It is one of several models which were tested in a series of studies [37] designed to explore hypersonic vehicle technology and provide data for computational fluid dynamic (CFD) code validation. The BWB heat-transfer and pressure model was tested experimentally in the Calspan shock tunnel [38] for a range of Mach and Reynolds numbers, at angles of attack from 0- to 10-*deg*. Heat-transfer measurements were made at over 100 surface locations and yielded distributions along the upper and lower symmetry planes, along off-centerline rays on the lower surface, and in the crossplane direction at several axial stations. The extensive database generated during these tests has been used for comparison [38–40] with several state-of-the-art computer codes. Comparisons are made with LAURA results for laminar flows over the BWB in reference 10. In the present study, calculations are performed for a Mach 19.6 perfect-gas case at 0-*deg* angle of attack. The freestream conditions are $\rho_\infty = 0.0066\ kg/m^3$ and $T_\infty = 240.9\ K$, with the wall temperature specified to be $T_w = 1256\ K$.

In reference 10, the surface of the vehicle was modeled using Cheatwood and DeJarnette's ASTUD (Advanced Surface-fitting Technique with User-friendly Development) interactive computer code [41, 42]. Since the calculations were to be terminated at the end of the compression ramp system ($z/L = 0.778$), only that portion of the geometry was modeled. Thus, the wings and vertical tail shown in figure 8 were not included in the surface model or subsequent computations. The 3-D volume grid is simply a collocation of orthogonal 2-D grids which were generated around cross sections of the BWB at 48 specified axial locations. In the circumferential direction, 64 cells were used. The resultant surface distribution is shown in figure 9. Note that the axial spacing clusters stations around the ramp junctures ($z/L = 0.435$ and $z/L = 0.560$). For each cross-sectional plane, the circumferential distribution of the cells is tied to the local body curvature.

Rather than beginning the computations for the present case from freestream values, a converged flowfield solution (and grid) from reference 10 is used as the initialization for the present case. As with the previous cases, the flowfield is solved for laminar flow initially, before the turbulence is "turned-on". The transition point is specified to be $s/L = .08$. Initially, 64 cells are used in the normal direction and this converged solution supplies the

initialization for an 80-cell solution. The heating rates from the two solutions are generally within five percent of one another, so another increase in the cell density in the normal direction is deemed unnecessary.

In addition to the body-surface cell distribution, figure 9 shows the converged flowfield grid (80-cell) at two of the cross-sectional planes. For visualization purposes, only the boundaries of every fourth cell in the normal direction are shown. It should be noted that, as for the equilibrium case, grid adjustment proved to be cumbersome.

As with the previous cases, the normalized heating rates (using both the Cebeci-Smith and Baldwin-Lomax models) are plotted as a function of nondimensional axial distance (where here, the axial distance is measured from virtual apex of the geometry rather than its blunted nose). Results are presented for the upper and lower symmetry plane, as well as three "off-centerline" rays on the lower surface. For selected axial stations, circumferential heating rates are plotted as a function of spanwise distance from the body centerline. Note that laminar heating-rate calculations are also presented for this case. Figure 10 provides a planform view of the lower surface of the body which shows the locations of the cross-sections and off-centerline rays where heat-transfer calculations are compared with experimental values.

Figure 11 shows the symmetry plane heating results for the upper and lower surface. Along the upper surface, the flow appears to remain laminar for the length of the body, although the rise in the experimental data at the end would seem to indicate the reattachment of a separated flow. On the lower surface, the flow is turbulent and both models predict the proper trends in the heating. However, the numerical results are consistently twenty to thirty percent higher than the data. The specified transition point may be premature, but that still doesn't explain the behavior for the length of the body. Similar results were seen in reference 10 for laminar flow along the lower centerline.

Figure 12 gives results along three off-centerline rays. Judging from the comparison with the data, the flow appears to remain laminar over the forebody in the regions away from the centerline, with a transition to turbulence occurring at the start of the first ramp. In contrast to the lower centerline results, the turbulent predictions along the off-centerline rays are in excellent agreement with the data (generally within ten percent). In reference 10 as well, agreement along these rays was better than along the centerline itself.

Turning to the circumferential heating distributions, figure 13 shows the heating near the nose where the flow is still laminar. As a result, the three curves are nearly identical and are generally within fifteen percent of the data. Figure 14 shows the heating rates at a station just after the specified transition point. The turbulent predictions are beginning their departure from the laminar solution. Agreement with the data is generally within ten percent, except for the lower symmetry plane as noted earlier.

Continuing downstream, figure 15 shows the heating-rate calculations at the next station where experimental data are available. It appears that the specified transition point is premature since the data more closely match the laminar solution at this station. In fact, excluding the upper symmetry plane, agreement between the laminar solution and the measurements is typically within ten percent. Values for the heating rates in figure 16 indicate the transition to turbulence has begun. Here, the lower centerline appears to be almost fully turbulent, although the majority of the flow at this station remains laminar.

Recall that this case is at 0-*deg* angle-of-attack. As a result, because of the shape of

the body, the upper surface heating has been higher than the lower surface heating at the stations considered thus far. Figure 17 shows results at a station within the "crossover" region, where the lower surface heating begins to exceed the upper surface heating. Still, beyond a small region adjacent to the lower centerline of the body, the flow appears to remain laminar. The turbulent prediction is within 25 percent of the measured value, while differences between the laminar results and the other data range from 15 percent on the lower surface to 40 percent on the upper.

The results shown in figure 18 are from a station located on the first ramp. It now appears that the entire lower surface has transitioned to turbulent flow, perhaps triggered by the surface discontinuity of the forebody-ramp juncture. Agreement between the predicted turbulent values and the experimental results is within ten percent except along the centerline. The upper surface appears to remain laminar, with disagreement between calculated and measured values ranging from 0 to 30 percent. The numerical solution does seem to model the general behavior quite well, and the possibility of scatter in the experimental data should not be dismissed. Figure 19 shows results for a station located on the second ramp. Again, the lower surface appears to be fully turbulent, and agreement between calculations and data ranges from five to fifteen percent. The upper surface is still laminar, although the rise in heating on the centerline is indicative of the reattachment of a separated flow.

The final station for comparison is presented in figure 20. As before, turbulent predictions agree well with the measured values on the ramp. The flow appears to be in transition in the area around the chine. On the upper surface, the separation/recirculation region is larger than at the previous station.

The shock-layer flowfield can be more easily visualized in figure 21, which is a flooded plot of the crossflow velocity for this same station. A region of freestream flow (zero crossflow) lies between the outer grid boundary and the captured bow shock. A region of outflow extends from the bow shock down into the boundary layer. The region of darkest shading corresponds to the region of inflow (the boundary between these two regions is denoted as the dividing streamline). For both the windward and leeward sides of the body, this region is indicative of circumferential growth in the boundary-layer thickness. With increasing boundary-layer thickness, the heating decreases because the magnitude of near-wall stresses is reduced. In this region of inflow on the windward surface, the calculated heating does decrease as seen in figures 18 through 20. The fact that the results do not match the windward experimental values would seem to indicate more cells in the circumferential direction are required to accurately predict the boundary-layer growth and subsequent heating in this region.

The circumferential boundary-layer growth is more dramatic on the leeward side (see figure 21). Separation occurs as indicated by the region very near the body where the flow changes direction again. This separation point corresponds to the point of minimum heating in figure 20. In the reattachment region, the heating rate increases from its minimum. From figure 20, it would appear that the flow in this region is in transition to turbulence, since the experimental data lie between the laminar and turbulent numerical results. However, without further study, it is impossible to say whether this discrepancy is in fact due to transition. It could be caused by inadequate grid resolution, use of the thin-layer rather than full Navier-Stokes equations, or shortcomings of the algebraic model as employed here.

Figure 21 offers an opportunity to elaborate on the shortcomings of the grid alignment

initialization for an 80-cell solution. The heating rates from the two solutions are generally within five percent of one another, so another increase in the cell density in the normal direction is deemed unnecessary.

In addition to the body-surface cell distribution, figure 9 shows the converged flowfield grid (80-cell) at two of the cross-sectional planes. For visualization purposes, only the boundaries of every fourth cell in the normal direction are shown. It should be noted that, as for the equilibrium case, grid adjustment proved to be cumbersome.

As with the previous cases, the normalized heating rates (using both the Cebeci-Smith and Baldwin-Lomax models) are plotted as a function of nondimensional axial distance (where here, the axial distance is measured from virtual apex of the geometry rather than its blunted nose). Results are presented for the upper and lower symmetry plane, as well as three "off-centerline" rays on the lower surface. For selected axial stations, circumferential heating rates are plotted as a function of spanwise distance from the body centerline. Note that laminar heating-rate calculations are also presented for this case. Figure 10 provides a planform view of the lower surface of the body which shows the locations of the cross-sections and off-centerline rays where heat-transfer calculations are compared with experimental values.

Figure 11 shows the symmetry plane heating results for the upper and lower surface. Along the upper surface, the flow appears to remain laminar for the length of the body, although the rise in the experimental data at the end would seem to indicate the reattachment of a separated flow. On the lower surface, the flow is turbulent and both models predict the proper trends in the heating. However, the numerical results are consistently twenty to thirty percent higher than the data. The specified transition point may be premature, but that still doesn't explain the behavior for the length of the body. Similar results were seen in reference 10 for laminar flow along the lower centerline.

Figure 12 gives results along three off-centerline rays. Judging from the comparison with the data, the flow appears to remain laminar over the forebody in the regions away from the centerline, with a transition to turbulence occurring at the start of the first ramp. In contrast to the lower centerline results, the turbulent predictions along the off-centerline rays are in excellent agreement with the data (generally within ten percent). In reference 10 as well, agreement along these rays was better than along the centerline itself.

Turning to the circumferential heating distributions, figure 13 shows the heating near the nose where the flow is still laminar. As a result, the three curves are nearly identical and are generally within fifteen percent of the data. Figure 14 shows the heating rates at a station just after the specified transition point. The turbulent predictions are beginning their departure from the laminar solution. Agreement with the data is generally within ten percent, except for the lower symmetry plane as noted earlier.

Continuing downstream, figure 15 shows the heating-rate calculations at the next station where experimental data are available. It appears that the specified transition point is premature since the data more closely match the laminar solution at this station. In fact, excluding the upper symmetry plane, agreement between the laminar solution and the measurements is typically within ten percent. Values for the heating rates in figure 16 indicate the transition to turbulence has begun. Here, the lower centerline appears to be almost fully turbulent, although the majority of the flow at this station remains laminar.

Recall that this case is at 0-*deg* angle-of-attack. As a result, because of the shape of

[6]P. A. Gnoffo, R. S. McCandless, and H. C. Yee. "Enhancements to Program LAURA for Computation of Three-Dimensional Hypersonic Flow". AIAA Paper 87-0280, January 1987.

[7]P. A. Gnoffo. "An Upwind-Biased Point-Implicit Relaxation Algorithm for Viscous, Compressible Perfect-Gas Flows". NASA TP 2953, June 1990.

[8]P. A. Gnoffo. "Upwind-Biased Point-Implicit Relaxation Strategies for Viscous Hypersonic Flows". AIAA Paper 89-1972, June 1989.

[9]F. A. Greene. "An Upwind-Biased Space Marching Algorithm for Supersonic Viscous Flow". NASA TP 3068, March 1991.

[10]R. A. Thompson and P. A. Gnoffo. "Application of the LAURA Code for Slender-Vehicle Aerothermodynamics". AIAA Paper 90-1714, June 1990.

[11]E. W. Miner, E. C. Anderson, and C. H. Lewis. "A Computer Program for Two-Dimensional and Axisymmetric Nonreacting Perfect Gas and Equilibrium Chemically Reacting Laminar, Transitional, and/or Turbulent Boundary Layer Flows". Technical Report VPI-E-71-8, Virginia Polytechnical Institute, May 1971.

[12]E. C. Anderson and J. N. Moss. "Numerical Solution of the Hypersonic Viscous-Shock-Layer Equations for Laminar, Transitional, and Turbulent Flows of a Perfect Gas Over Blunt Axially Symmetric Bodies". NASA TN D-7865, February 1975.

[13]T. J. Coakley. "Turbulence Modeling Methods for the Compressible Navier-Stokes Equations". AIAA Paper 83-1693, July 1983.

[14]T. Cebeci and A. M. O. Smith. "A Finite-Difference Solution to the Incompressible Turbulent Boundary Layer Equations by an Eddy Viscosity Concept". In *Computation of Turbulent Boundary Layers, Volume 1*, pages 346–355. AFOSR-IFP-Stanford Conference, Stanford University, 1968.

[15]T. Cebeci. "Behavior of Turbulent Flow near a Porous Wall with Pressure Gradient". *AIAA Journal*, volume 8 : pp. 2152–2156, December 1970.

[16]T. Cebeci and A. M. O. Smith. "A Finite-Difference Method for Calculating Compressible Laminar and Turbulent Boundary Layers". *Journal of Basic Engineering*, pages 523–535, September 1970.

[17]B. S. Baldwin and H. Lomax. "Thin Layer Approximation and Algebraic Model for Separated Turbulent Flows". AIAA Paper 78-0257, January 1978.

[18]L. A. King and D. A. Johnson. "Separated Transonic Airfoil Flow Calculations with a Nonequilibrium Turbulence Model". NASA TM 86830, 1985.

[19]H. C. Yee. "On Symmetric and Upwind TVD Schemes". NASA TM 86842, 1955.

[20]P. L. Roe. "Approximate Riemann Solvers, Parameter Vectors, and Difference Schemes". *Journal of Computational Physics*, volume 43 (number 2): pp. 357–372, October 1981.

[21]J. C. Adams, Jr. "Analysis of the Three-Dimensional Compressible Turbulent Boundary Layer on a Sharp Cone at Incidence in Supersonic and Hypersonic Flow". Technical Report AEDC-TR-72-66, von Karmon Gas Dynamics Facility, Arnold Engineering Development Center, June 1972.

[22]E. R. Van Driest. "On Turbulent Flow Near a Wall". *Journal of Aeronautical Sciences*, volume 23 (number 11): pp. 1007–1011, November 1956.

[23]F. H. Clauser. "The Turbulent Boundary Layer". In H. L. Dryden and T. von Karmen,

editors, *Vol. IV of Advances in Applied Mechanics*, pages 1–15. Academic Press, New York, 1956.

[24]P. S. Klebanoff. "Characteristics of Turbulence in a Boundary Layer with Zero Pressure Gradient". NACA Report 1247, 1955.

[25]R. N. Gupta, K. P. Lee, E. V. Zoby, J. N. Moss, and R. A. Thompson. "Hypersonic Viscous Shock-Layer Solutions over Long Slender Bodies–Part I: High Reynolds Number Flows". *Journal of Spacecraft and Rockets*, volume 27 (number 2): pp. 175–184, March-April 1990.

[26]S. Dhawan and R. Narashima. "Some Properties of Boundary Layer Flow during Transition from Laminar to Turbulent Motion". *Journal of Fluid Mechanics*, volume 1 (Part 4): pp. 418–436, January 1958.

[27]J. E. Harris. "Numerical Solutions of the Equations for Compressible Laminar, Transitional and Turbulent Boundary Layers and Comparisons with Experimental Data". NASA TR 368, 1971.

[28]P. A. Gnoffo, L. C. Hartung, and R. B. Greendyke. "Heating Analysis for a Lunar Transfer Vehicle at Near-Equilibrium Conditions". AIAA Paper 93-0270, January 1993.

[29]M. D. Jackson and D. L. Baker. "Passive Nosetip Technology (PANT) Program. Volume 3. Surface Roughness Effects, Part 1: Experimental Data". Technical Report SAMSO-TR-74-86-VOL-3-PT-1, ACUREX Corporation, January 1974.

[30]F. M. Cheatwood and F. R. DeJarnette. "An Approximate Viscous Shock Layer Approach to Calculating Hypersonic Flows about Blunt-Nosed Bodies". AIAA Paper 91-1348, June 1991.

[31]R. T. Davis. "Numerical Solution of the Hypersonic Viscous Shock Layer Equations". *AIAA Journal*, volume 8 (number 5): pp. 843–851, May 1970.

[32]S. H. Maslen. "Inviscid Hypersonic Flow Past Smooth Symmetric Bodies". *AIAA Journal*, volume 5 : pp. 1055–1061, June 1964.

[33]F. M. Cheatwood and F. R. DeJarnette. "An Approximate Viscous Shock Layer Technique for Calculating Chemically Reacting Hypersonic Flows about Blunt-Nosed Bodies". NASA CR 187617, August 1991.

[34]C. F. Hansen. "Approximations for the Thermodynamic and Transport Properties of High Temperature Air". NASA TR R-50, 1959.

[35]S. Srinivasan, J. C. Tannehill, and K. J. Weilmuenster. "Simplified Curve Fits for the Thermodynamic Properties of Equilibrium Air". NASA RP 1181, August 1987.

[36]S. Srinivasan and J. C. Tannehill. "Simplified Curve Fits for the Transport Properties of Equilibrium Air". NASA CR 178411, December 1987.

[37]McDonnell Douglas Corporation. "Generic Technology Option #2–CFD Code Validation: Fourth Quarterly Review". Technical report, October 6 1987.

[38]K. Y. Lau and R. R. Cosner. "Generic Technology Option #2–Final Report; Volume IV–Blended Wing-Body Aerothermal Model and Test Program". Technical report, McDonnell Douglas Corporation, July 1 1988.

[39]P. F. Richardson, E. B. Parlette, J. Morrison, G. Switzer, and D. Dilley. "Heat Transfer and Pressure Comparisons Between Computation and Wind Tunnel for a Research Hypersonic Aircraft". AIAA Paper 89-0029, January 1989.

[40]W. J. Krawczyk. "Analysis of Aerospace Vehicle Scramjet Propulsive Flow Fields: 3-D Forebody Code Development". NASP Contractor Report 1029, November 1988.

editors, *Vol. IV of Advances in Applied Mechanics*, pages 1–15. Academic Press, New York, 1956.

[24]P. S. Klebanoff. "Characteristics of Turbulence in a Boundary Layer with Zero Pressure Gradient". NACA Report 1247, 1955.

[25]R. N. Gupta, K. P. Lee, E. V. Zoby, J. N. Moss, and R. A. Thompson. "Hypersonic Viscous Shock-Layer Solutions over Long Slender Bodies–Part I: High Reynolds Number Flows". *Journal of Spacecraft and Rockets*, volume 27 (number 2): pp. 175–184, March-April 1990.

[26]S. Dhawan and R. Narashima. "Some Properties of Boundary Layer Flow during Transition from Laminar to Turbulent Motion". *Journal of Fluid Mechanics*, volume 1 (Part 4): pp. 418–436, January 1958.

[27]J. E. Harris. "Numerical Solutions of the Equations for Compressible Laminar, Transitional and Turbulent Boundary Layers and Comparisons with Experimental Data". NASA TR 368, 1971.

[28]P. A. Gnoffo, L. C. Hartung, and R. B. Greendyke. "Heating Analysis for a Lunar Transfer Vehicle at Near-Equilibrium Conditions". AIAA Paper 93-0270, January 1993.

[29]M. D. Jackson and D. L. Baker. "Passive Nosetip Technology (PANT) Program. Volume 3. Surface Roughness Effects, Part 1: Experimental Data". Technical Report SAMSO-TR-74-86-VOL-3-PT-1, ACUREX Corporation, January 1974.

[30]F. M. Cheatwood and F. R. DeJarnette. "An Approximate Viscous Shock Layer Approach to Calculating Hypersonic Flows about Blunt-Nosed Bodies". AIAA Paper 91-1348, June 1991.

[31]R. T. Davis. "Numerical Solution of the Hypersonic Viscous Shock Layer Equations". *AIAA Journal*, volume 8 (number 5): pp. 843–851, May 1970.

[32]S. H. Maslen. "Inviscid Hypersonic Flow Past Smooth Symmetric Bodies". *AIAA Journal*, volume 5 : pp. 1055–1061, June 1964.

[33]F. M. Cheatwood and F. R. DeJarnette. "An Approximate Viscous Shock Layer Technique for Calculating Chemically Reacting Hypersonic Flows about Blunt-Nosed Bodies". NASA CR 187617, August 1991.

[34]C. F. Hansen. "Approximations for the Thermodynamic and Transport Properties of High Temperature Air". NASA TR R-50, 1959.

[35]S. Srinivasan, J. C. Tannehill, and K. J. Weilmuenster. "Simplified Curve Fits for the Thermodynamic Properties of Equilibrium Air". NASA RP 1181, August 1987.

[36]S. Srinivasan and J. C. Tannehill. "Simplified Curve Fits for the Transport Properties of Equilibrium Air". NASA CR 178411, December 1987.

[37]McDonnell Douglas Corporation. "Generic Technology Option #2–CFD Code Validation: Fourth Quarterly Review". Technical report, October 6 1987.

[38]K. Y. Lau and R. R. Cosner. "Generic Technology Option #2–Final Report; Volume IV–Blended Wing-Body Aerothermal Model and Test Program". Technical report, McDonnell Douglas Corporation, July 1 1988.

[39]P. F. Richardson, E. B. Parlette, J. Morrison, G. Switzer, and D. Dilley. "Heat Transfer and Pressure Comparisons Between Computation and Wind Tunnel for a Research Hypersonic Aircraft". AIAA Paper 89-0029, January 1989.

[40]W. J. Krawczyk. "Analysis of Aerospace Vehicle Scramjet Propulsive Flow Fields: 3-D Forebody Code Development". NASP Contractor Report 1029, November 1988.

[41]F. M. Cheatwood, F. R. DeJarnette, and H. H. Hamilton II. "An Interactive User-Friendly Approach to Surface-Fitting Three-Dimensional Geometries". NASA CR 4126, March 1988.

[42]F. M. Cheatwood, F. R. DeJarnette, and H. H. Hamilton II. "Interactive Approach to Surface Fitting Complex Geometries for Flowfield Applications". *Journal of Spacecraft and Rockets*, volume 26 (number 1): pp. 31–38, January-February 1989.

Table 1. Maximum cell stretching as a function of K_{str}.

K	K_{str}	$1 + f_{str}$
64	32	1.7
64	40	1.5
80	48	1.4
96	64	1.28
128	64	1.25

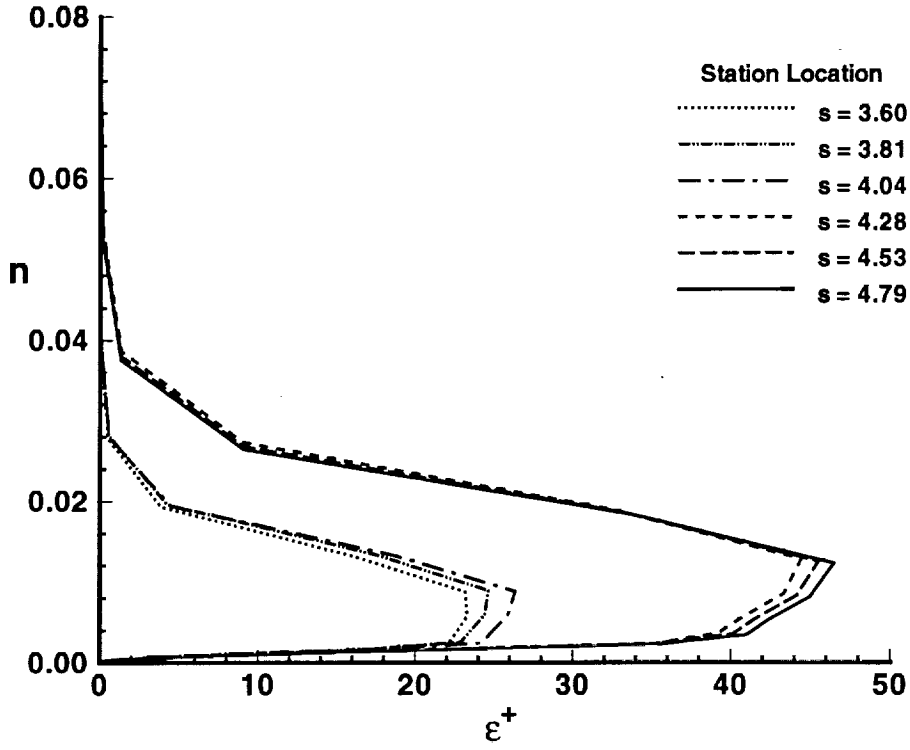

a) No smoothing

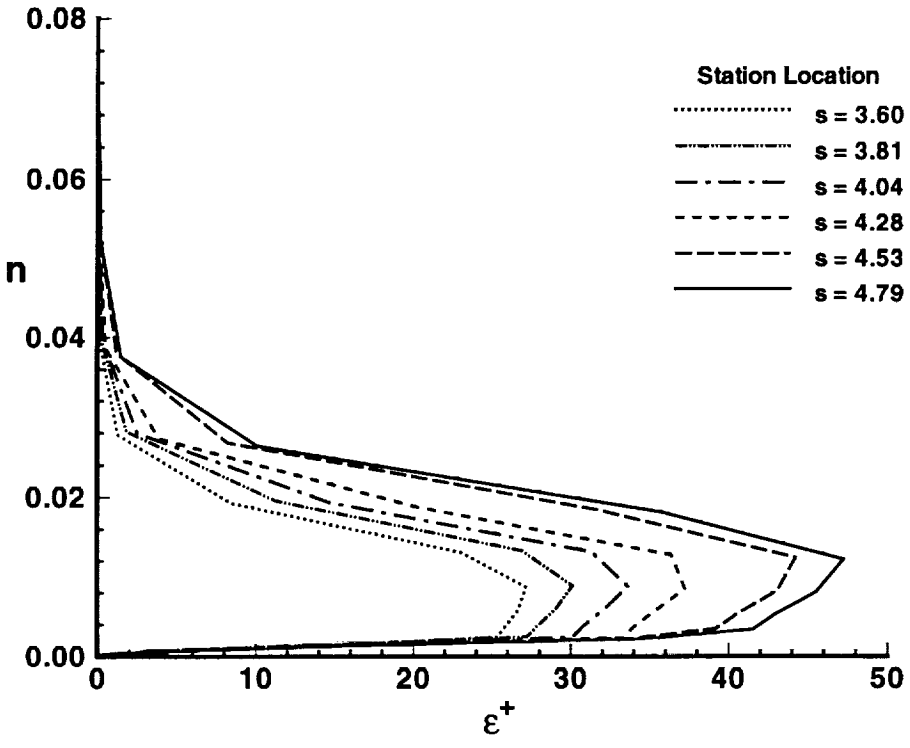

b) With parabolic blending

Figure 3. Near-body distribution of ε^+ in vicinity of jump.

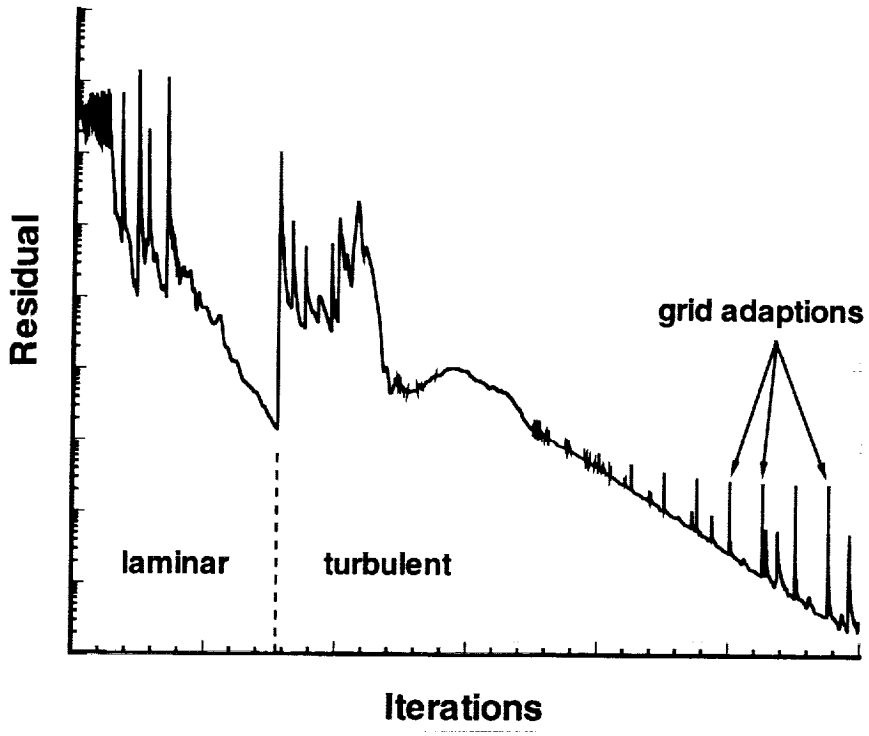

Figure 4. Typical residual history for LAURA solution.

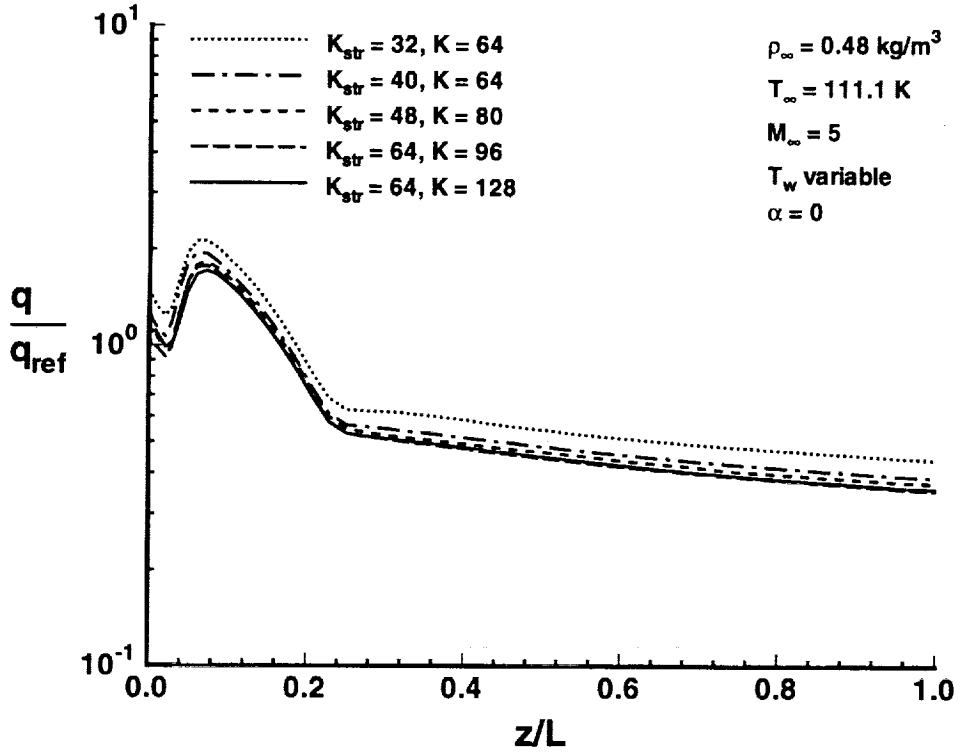

Figure 5. Grid-refinement study for 8-*deg* sphere-cone, $R_{nose} = 6.35cm\ (2.5in)$.

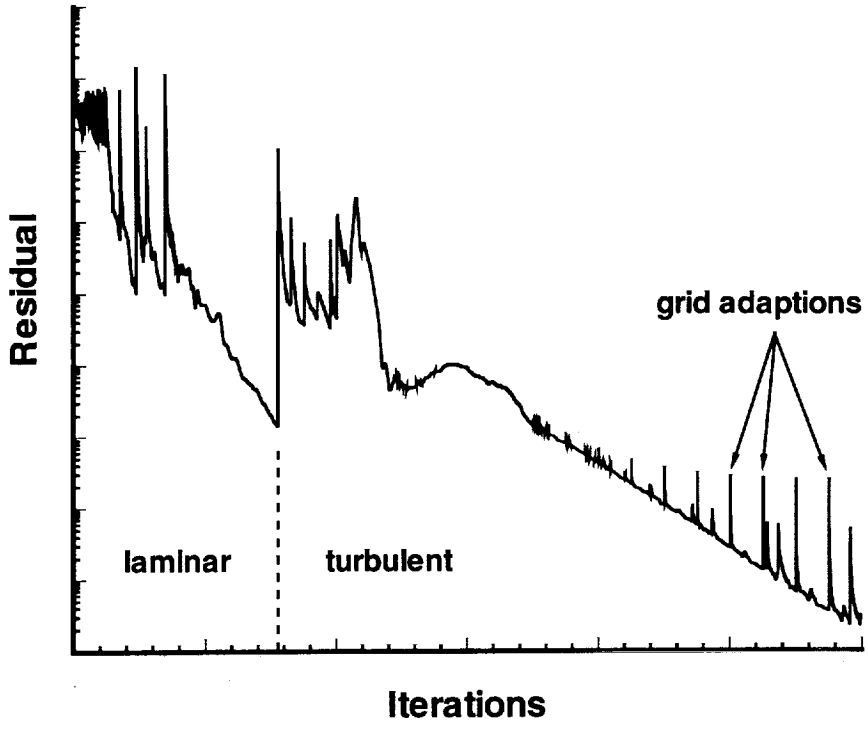

Figure 4. Typical residual history for LAURA solution.

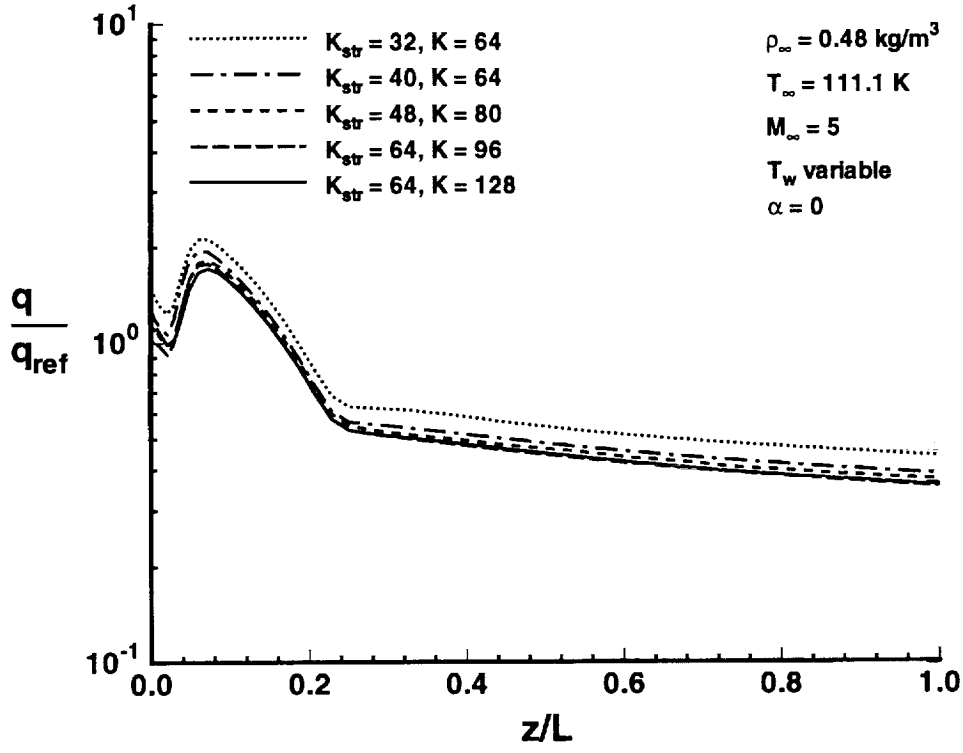

Figure 5. Grid-refinement study for 8-*deg* sphere-cone, $R_{nose} = 6.35cm\ (2.5in)$.

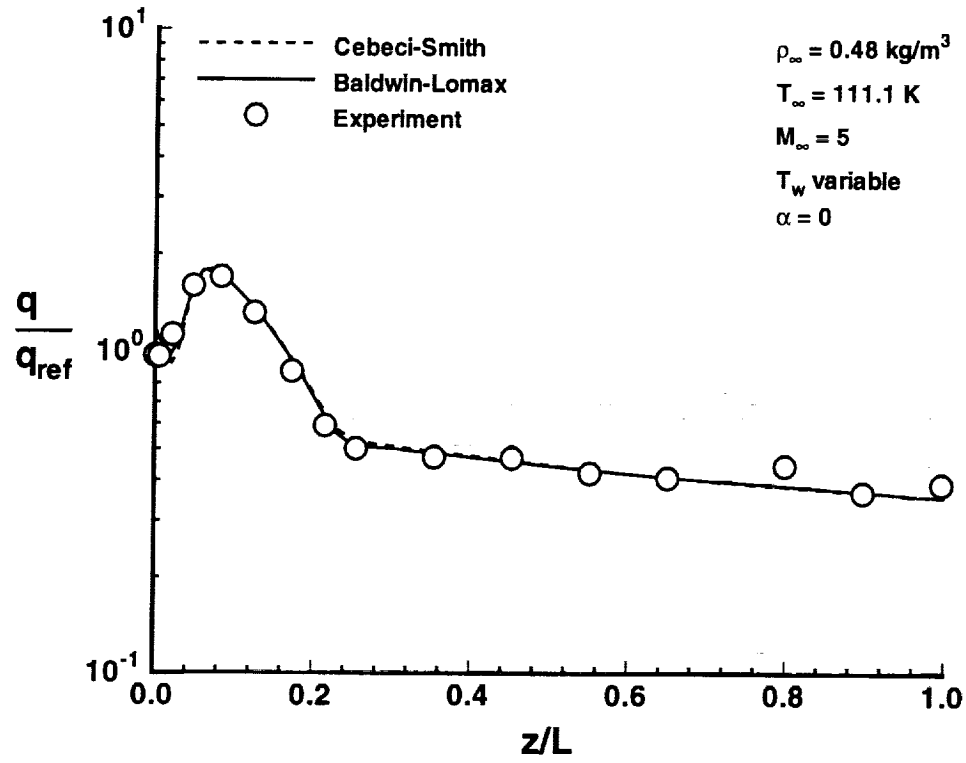

Figure 6. Heat-transfer results for 8-*deg* sphere-cone, $R_{nose} = 6.35cm\ (2.5in)$.

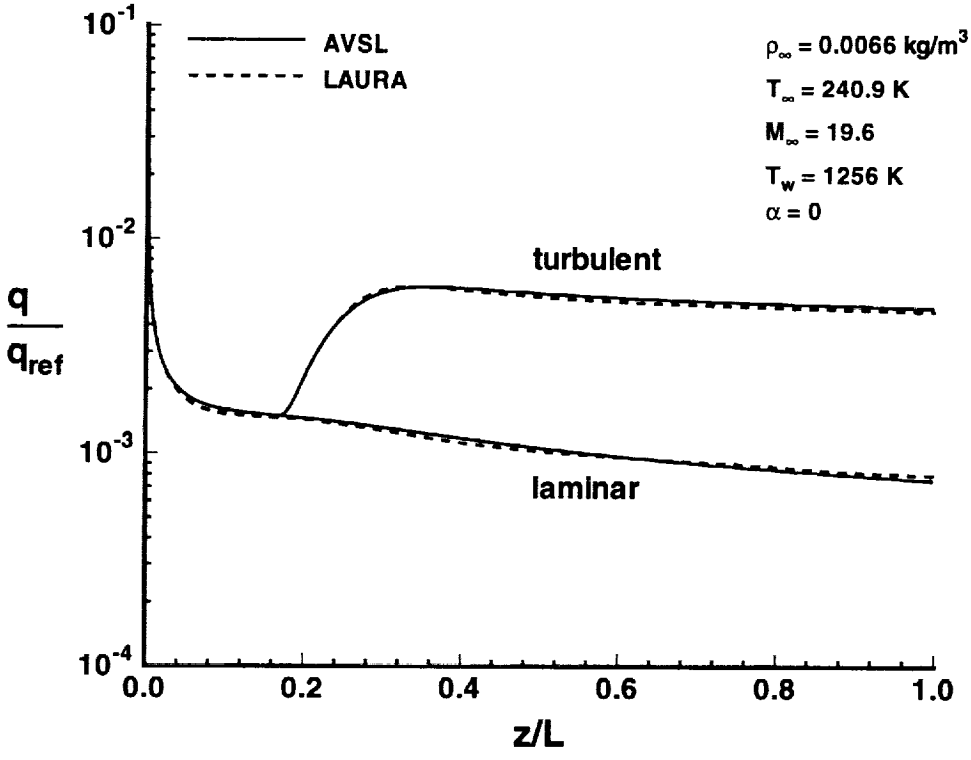

Figure 7. Heat-transfer results for 5-*deg* sphere-cone, $R_{nose} = 3.81cm\ (1.5in)$.

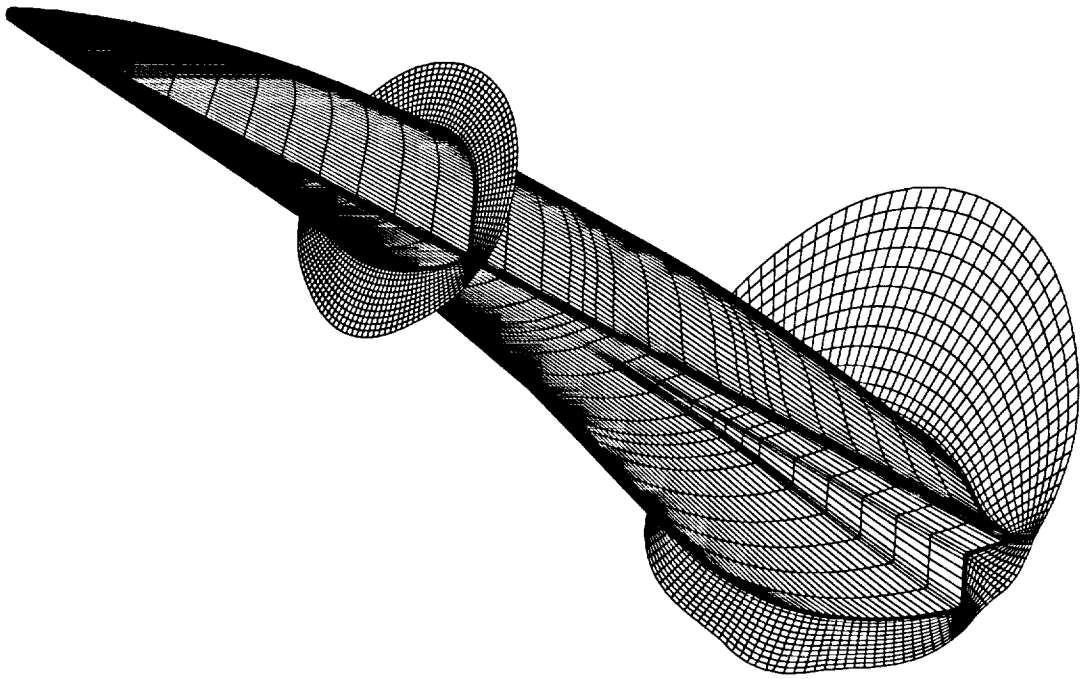

Figure 9. Flowfield and body-surface grids for blended wing-body.

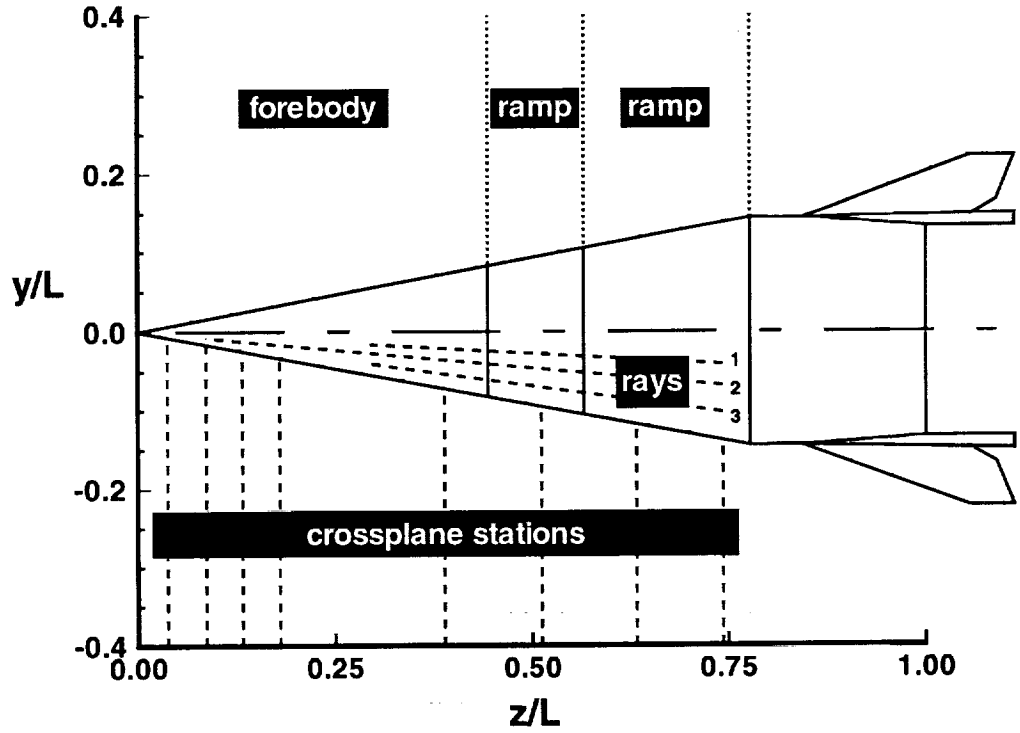

Figure 10. Lower planform view of blended wing-body.

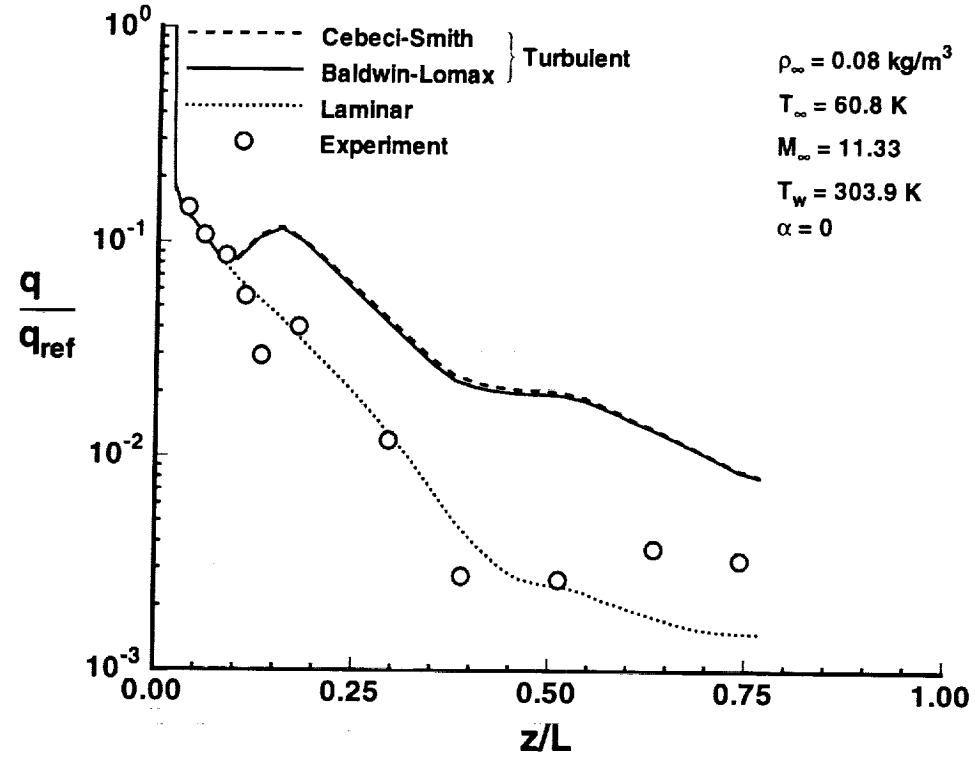

a) Upper surface

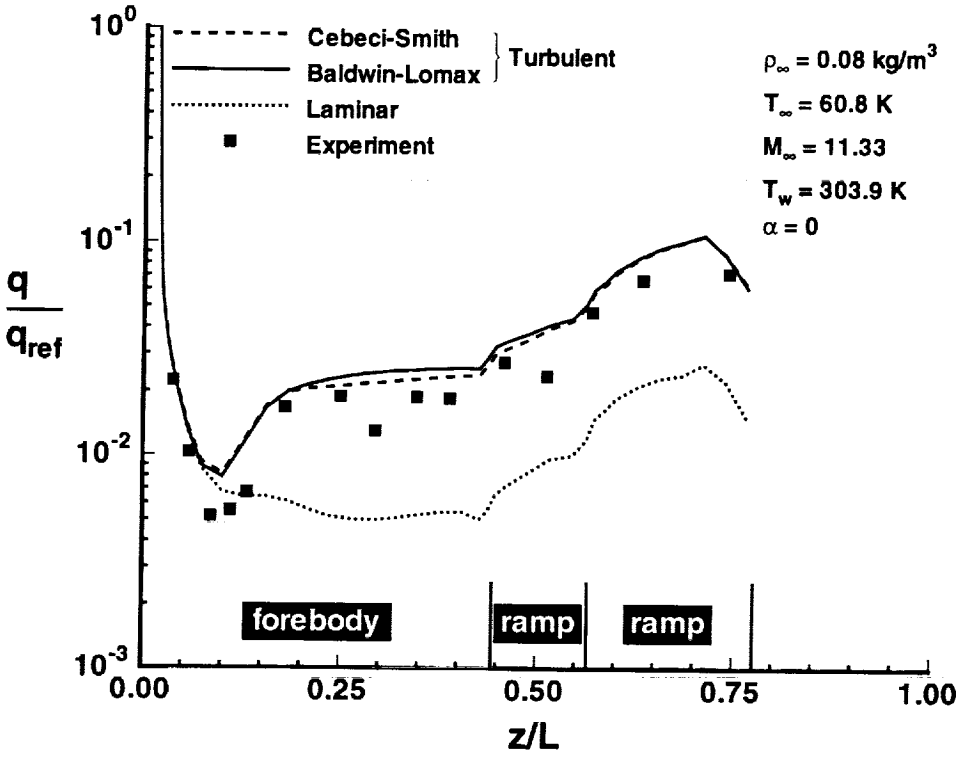

b) Lower surface

Figure 11. Symmetry plane heat-transfer results for the blended wing-body.

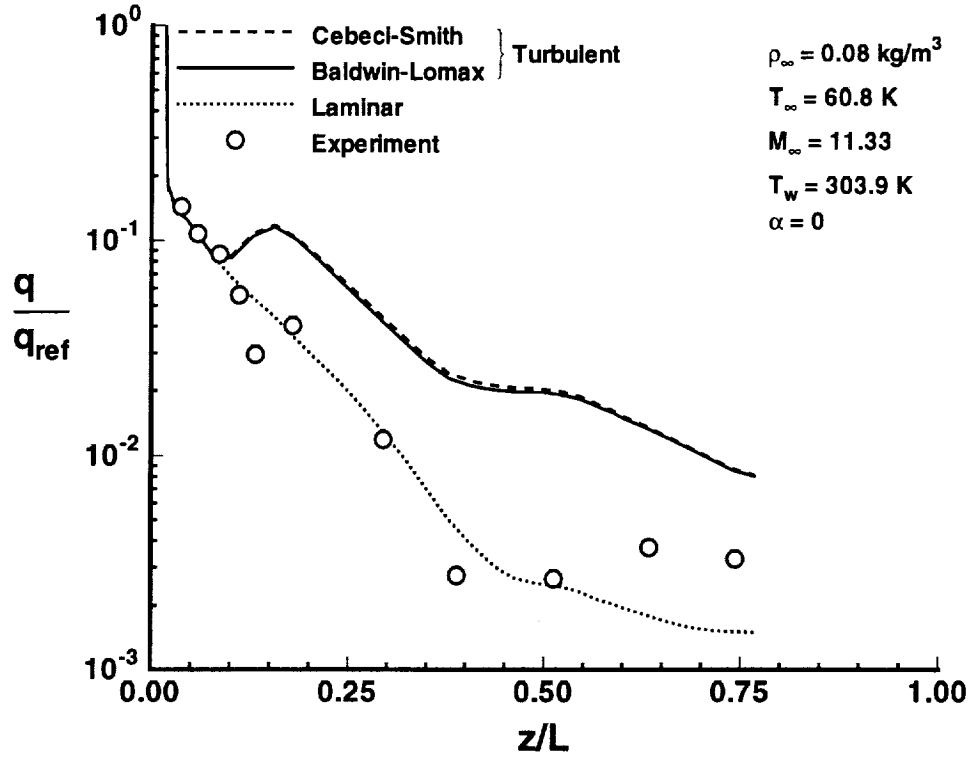

a) Upper surface

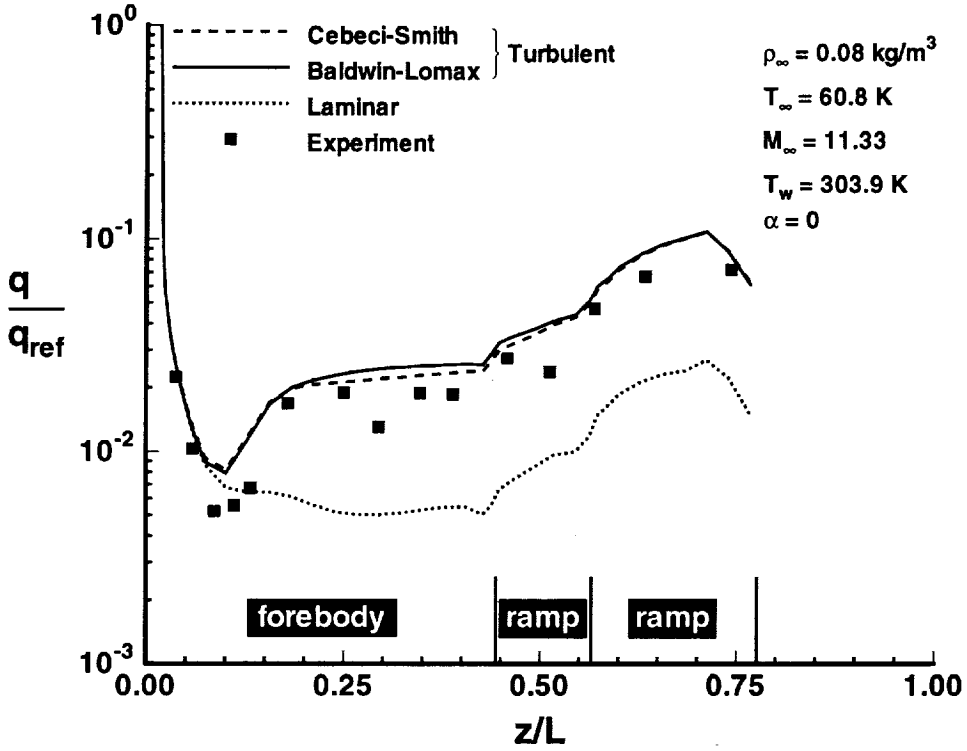

b) Lower surface

Figure 11. Symmetry plane heat-transfer results for the blended wing-body.

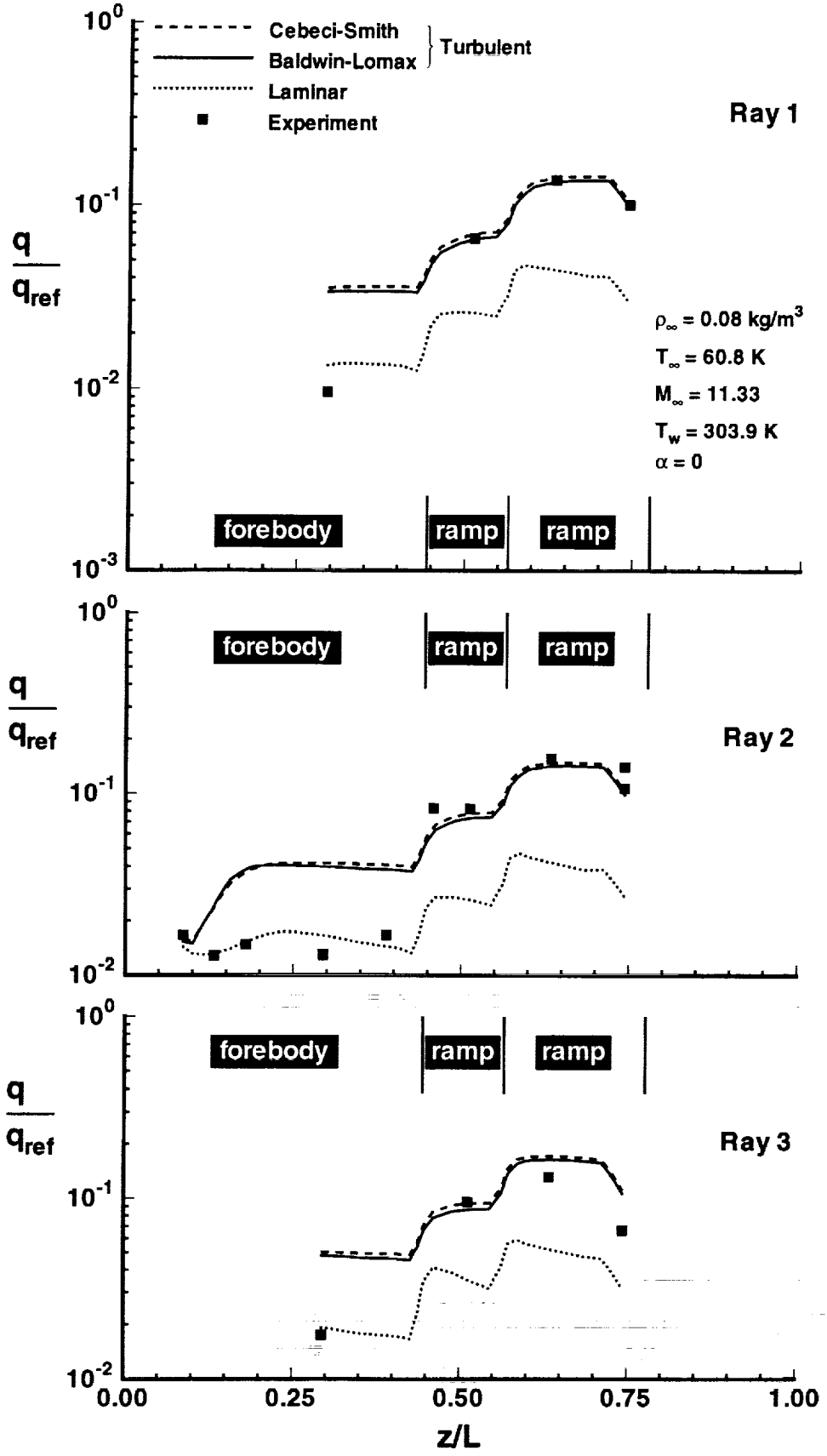

Figure 12. Off-centerline heat-transfer results for the blended wing-body.

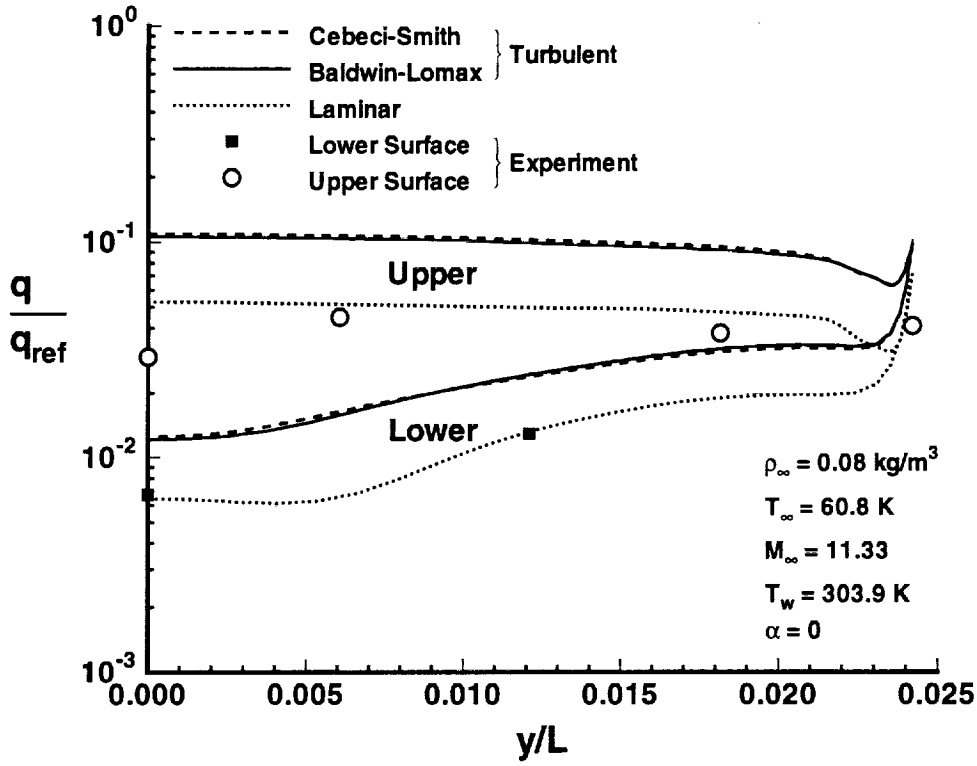

Figure 15. Crossplane ($z/L = 0.132$) heat-transfer results for the blended wing-body.

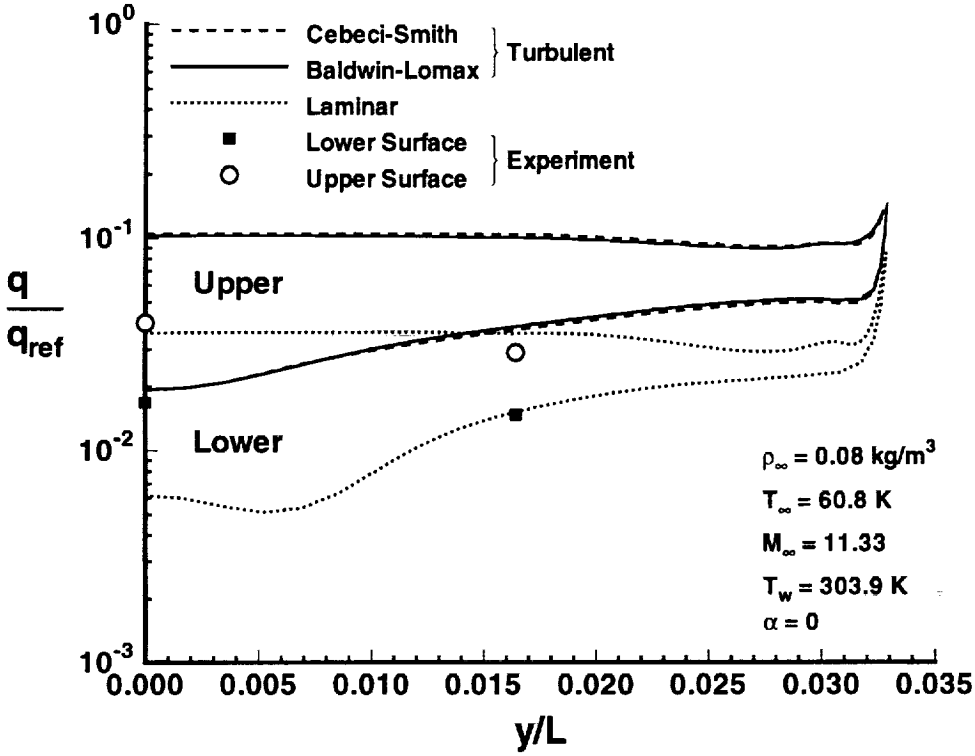

Figure 16. Crossplane ($z/L = 0.179$) heat-transfer results for the blended wing-body.

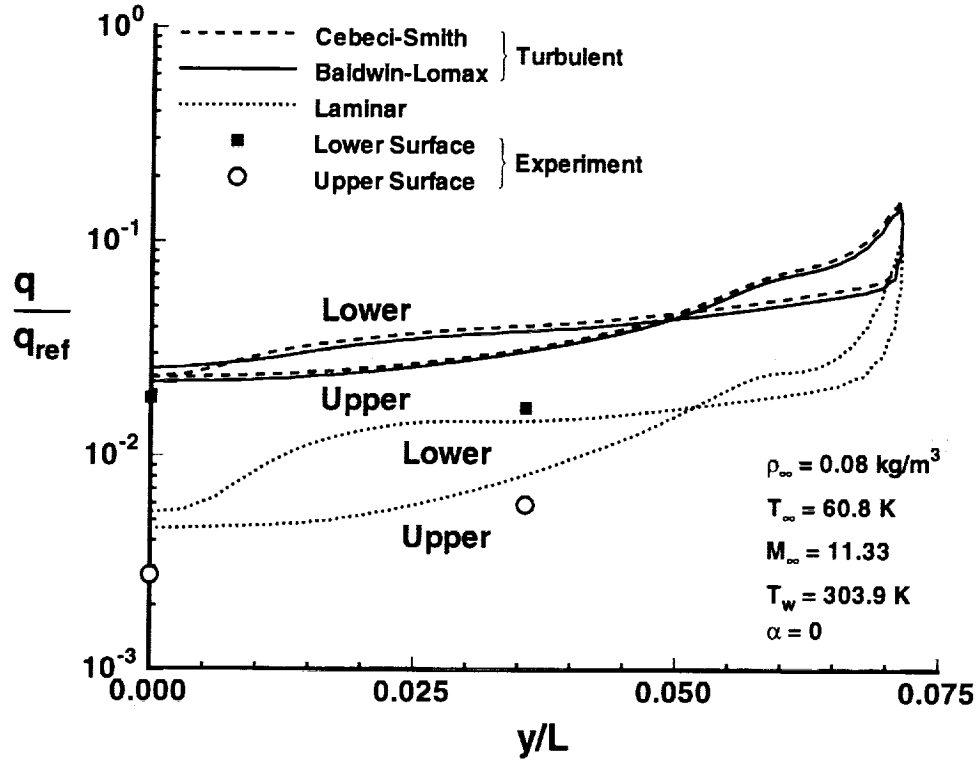

Figure 17. Crossplane ($z/L = 0.389$) heat-transfer results for the blended wing-body.

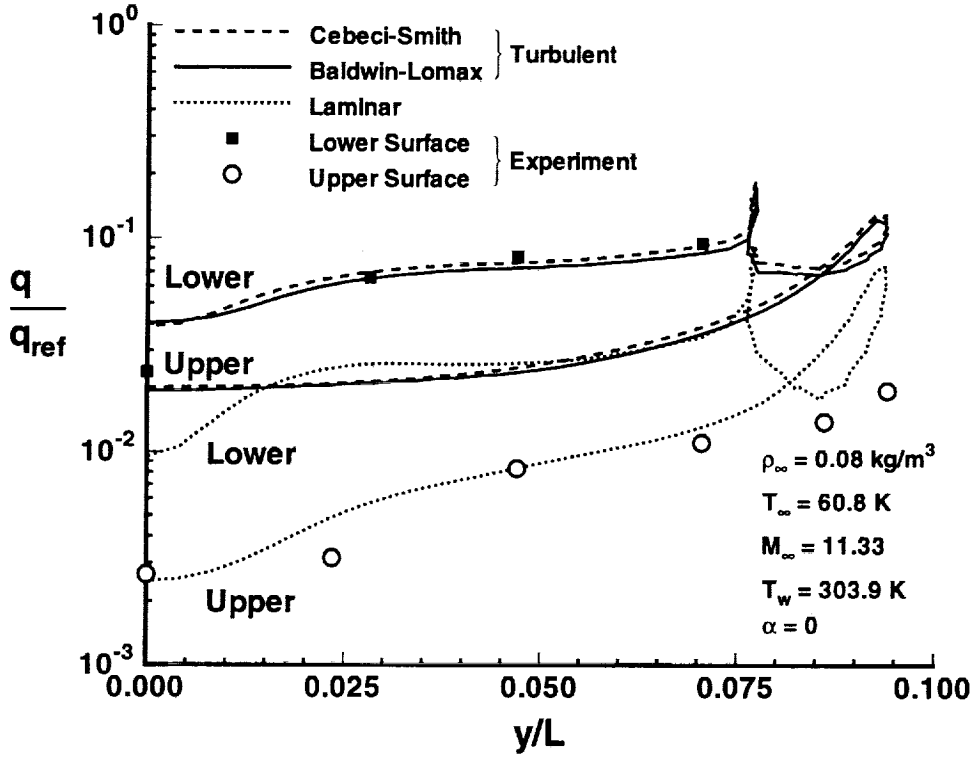

Figure 18. Crossplane ($z/L = 0.513$) heat-transfer results for the blended wing-body.

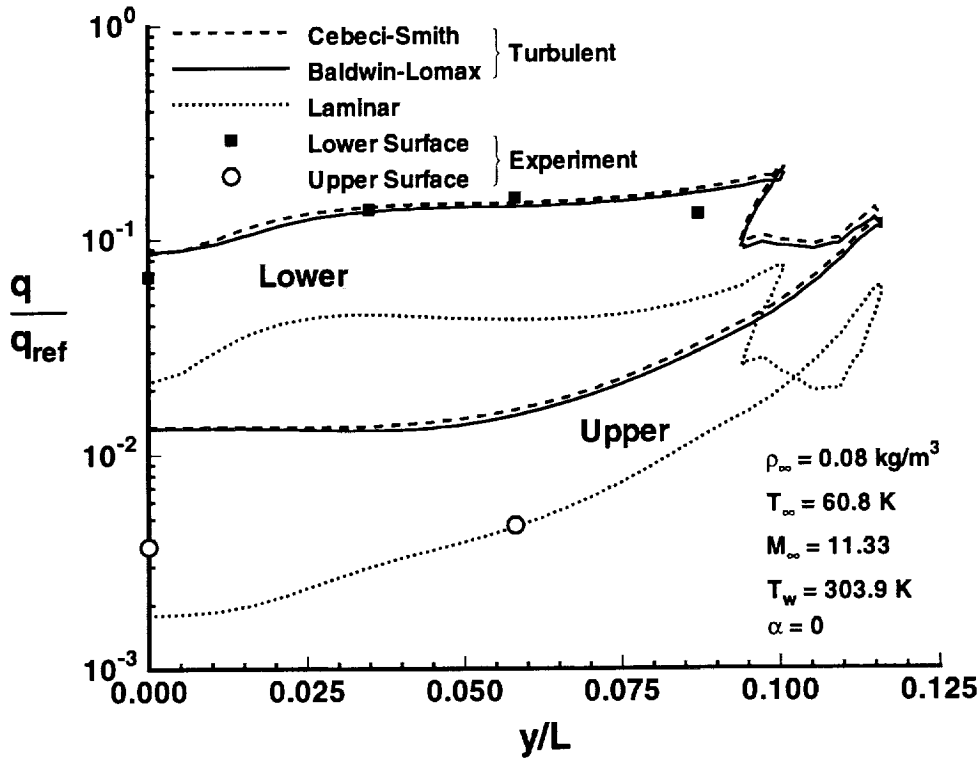

Figure 19. Crossplane ($z/L = 0.633$) heat-transfer results for the blended wing-body.

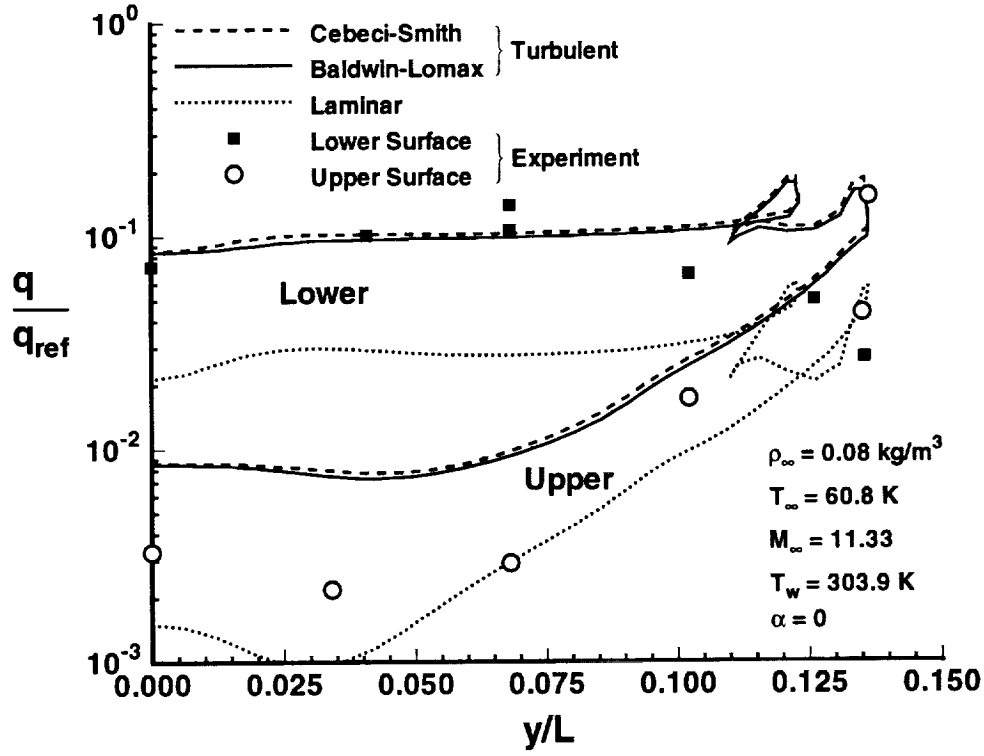

Figure 20. Crossplane ($z/L = 0.743$) heat-transfer results for the blended wing-body.

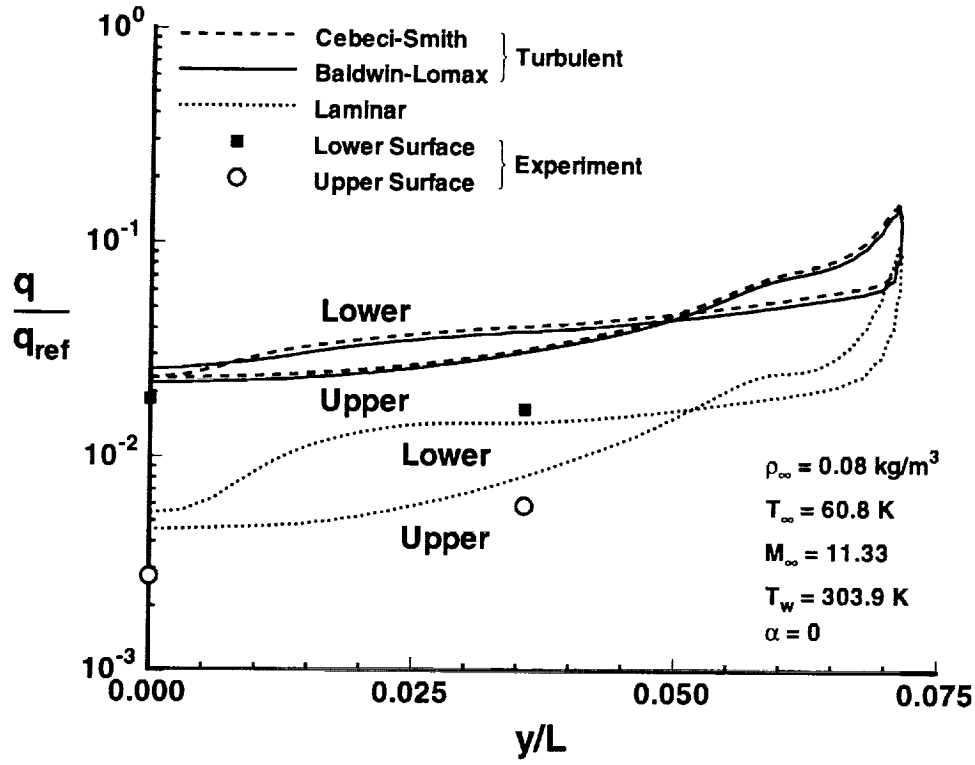

Figure 17. Crossplane ($z/L = 0.389$) heat-transfer results for the blended wing-body.

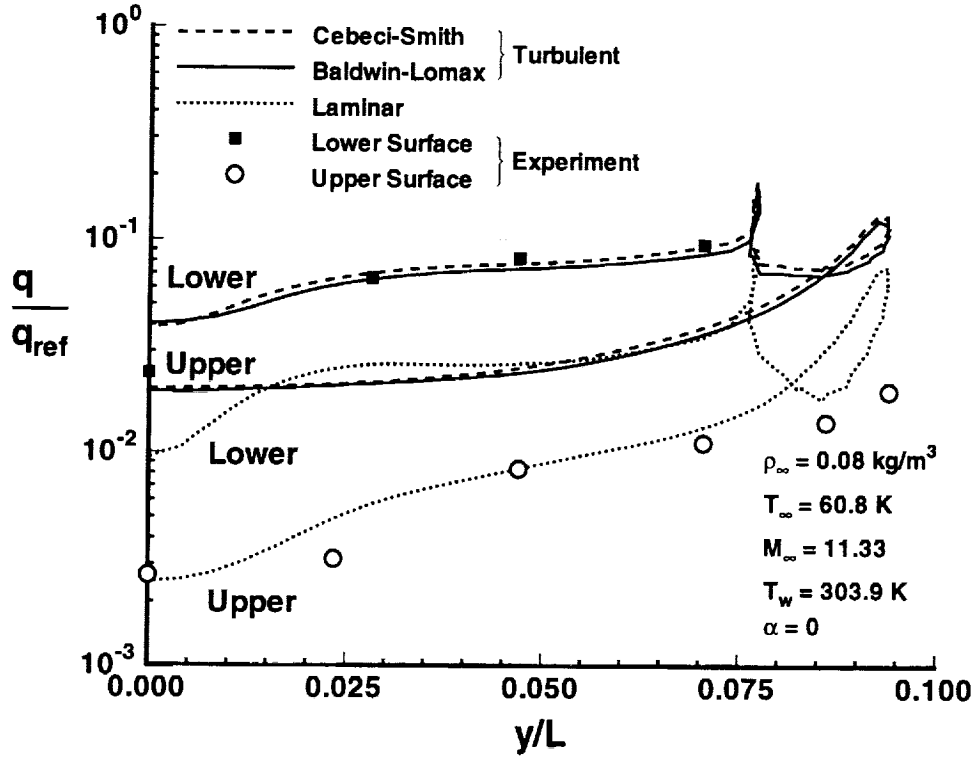

Figure 18. Crossplane ($z/L = 0.513$) heat-transfer results for the blended wing-body.

REPORT DOCUMENTATION PAGE

Form Approved
OMB No. 0704-0188

1. AGENCY USE ONLY *(Leave blank)*	2. REPORT DATE	3. REPORT TYPE AND DATES COVERED
	April 1993	Technical Memorandum

4. TITLE AND SUBTITLE
The Addition of Algebraic Turbulence Modeling to Program LAURA

5. FUNDING NUMBERS
WU 506-40-91-01

6. AUTHOR(S)
F. McNeil Cheatwood and R. A. Thompson

7. PERFORMING ORGANIZATION NAME(S) AND ADDRESS(ES)
NASA Langley Research Center
Hampton, VA 23681-0001

8. PERFORMING ORGANIZATION REPORT NUMBER

9. SPONSORING/MONITORING AGENCY NAME(S) AND ADDRESS(ES)
National Aeronautics and Space Administration
Washington, DC 20546-0001

10. SPONSORING/MONITORING AGENCY REPORT NUMBER
NASA TM-107758

11. SUPPLEMENTARY NOTES
Cheatwood: ViGYAN, Inc., Hampton, VA; and Thompson: Langley Research Center, Hampton, VA.

12a. DISTRIBUTION/AVAILABILITY STATEMENT
Unclassified Unlimited

Subject Category 34

12b. DISTRIBUTION CODE

13. ABSTRACT *(Maximum 200 words)*
The Langley Aerothermodynamic Upwind Relaxation Algorithm (LAURA) is modified to allow the calculation of turbulent flows. This is accomplished using the Cebeci-Smith and Baldwin-Lomax eddy-viscosity models in conjunction with the thin-layer Navier-Stokes options of the program. Turbulent calculations can be performed for both perfect-gas and equilibrium flows. However, a requirement of the models is that the flow be attached. It is seen that for slender bodies, adequate resolution of the boundary-layer gradients may require more cells in the normal direction than a laminar solution, even when grid stretching is employed. Results for axisymmetric and three-dimensional flows are presented. Comparison with experimental data and other numerical results reveal generally good agreement, except in the regions of detached flow.

14. SUBJECT TERMS
LAURA, perfect-gas,and Navier-Stokes

15. NUMBER OF PAGES
33

16. PRICE CODE
A03

17. SECURITY CLASSIFICATION OF REPORT	18. SECURITY CLASSIFICATION OF THIS PAGE	19. SECURITY CLASSIFICATION OF ABSTRACT	20. LIMITATION OF ABSTRACT
Unclassified	Unclassified		